

Contents lists available at ScienceDirect

# Mechanical Systems and Signal Processing

journal homepage: www.elsevier.com/locate/ymssp





# Empirical Fourier decomposition: An accurate signal decomposition method for nonlinear and non-stationary time series analysis

Wei Zhou a,b, Zhongren Feng a,c, Y.F. Xu b,\*, Xiongjiang Wang a, Hao Lv a

- <sup>a</sup> School of Civil Engineering and Architecture, Wuhan University of Technology, Wuhan 430070, PR China
- <sup>b</sup> Department of Mechanical and Materials Engineering, University of Cincinnati, Cincinnati, OH 45221, USA
- <sup>c</sup> School of Urban Construction, Wuchang Shouyi University, Wuhan 430064, PR China

#### ARTICLE INFO

# Keywords: Signal decomposition Empirical Fourier decomposition Empirical wavelet transform Fourier decomposition method Zero-phase filter bank

#### ABSTRACT

Signal decomposition is an effective tool to assist identification of modal information in timedomain signals. Two signal decomposition methods, including the empirical wavelet transform (EWT) and Fourier decomposition method (FDM), have been developed based on Fourier theory. However, the EWT can suffer from a mode mixing problem for signals with closely-spaced modes and from a trivial component problem resulting in a trivial residual in the first decomposed component. Decomposition results by FDM can suffer from an inconsistency problem. In this work, an accurate adaptive signal decomposition method, called the empirical Fourier decomposition (EFD), is proposed to solve the aforementioned problems. The proposed EFD combines the uses of an improved Fourier spectrum segmentation technique and a zero-phase filter bank. The segmentation technique solves the trivial component problem by an adaptive sorting process and the inconsistency problem by predefining the number of components in a signal to be decomposed. The zero-phase filter bank has no transition phases, which exist in the EWT, in its each filter function, and it can solve the mode mixing problem. Numerical investigations are conducted to study the effectiveness and accuracy of the EFD. It is shown that the EFD can yield accurate and consistent decomposition results for signals with multiple non-stationary modes and those with closely-spaced modes, compared with decomposition results by the EWT, FDM, variational mode decomposition and empirical mode decomposition. It is also shown that the EFD can yield accurate time-frequency representation results and it has the highest computational efficiency among the compared decomposition methods. An experimental validation is also conducted to study the effectiveness of the EFD for experimentally measured signals with closelyspaced modes. It is shown that the EFD can decompose a signal with closely-spaced modes with higher accuracy, compared with the other decomposition methods.

#### 1. Introduction

Signal decomposition is a widely used numerical tool in different fields, such as biomedical signal analysis [1], seismic signal

<sup>\*</sup> Corresponding author.

E-mail addresses: zhouw6@mail.uc.edu (W. Zhou), fengz515@163.com (Z. Feng), xu2yf@uc.edu (Y.F. Xu), wangxiongjiang@whut.edu.cn (X. Wang), liberty.hunter@whut.edu.cn (H. Lv).

analysis [2], mechanical vibration signal analysis [3,4], and speech enhancement [5]. Time-domain signals that derive from a physical system usually comprise several superposed components, which are referred to as modes [6], and the modes can encompass meaningful frequency-domain information of the signals, referred to as modal information. Hence, it is crucial to obtain signal decomposition results with high accuracy and efficiency.

In the past few decades, several signal decomposition methods have been developed, and the empirical mode decomposition (EMD) [7] is one of the most significant methods, even though its mathematical understanding is limited and it has some known shortcomings, such as robustness of mode mixing [8] and end effects [9]. Improved versions of the EMD have been developed to overcome the shortcomings. The ensemble EMD [10] has been developed by adding white noise with finite amplitudes to alleviate the mode mixing and end effects problems. The complete ensemble EMD [11] has been developed to further improve the EMD by adding completeness and a full data-driven number of modes, which are missing in the ensemble EMD. Permutation entropy has been introduced by Zheng et al. [12] to quantify intermittency and noise in a signal to be decomposed by the partly ensemble EMD, by which fewer false components are obtained in decomposition results than those by the ensemble EMD and complete ensemble EMD. Lang et al. [13] replaced the mean operator with the median operator in the ensemble EMD to solve the mode splitting problem in the ensemble EMD [14]. Li et al. presented a time-varying filter technique to solve the mode mixing problem [15]. However, these EMD methods cannot fundamentally solve the mode mixing and end effects problems. The variational mode decomposition (VMD) [16] is a non-recursive signal decomposition method, which has been developed based on a generalization of Wiener filters. Recently, the successive VMD has been developed by adding several criteria to ensure that modes of interest do not or less overlap with other modes in decomposition results [17]. The added criteria in the successive VMD can eliminate the requirement of predefining the number of components in a signal to be decomposed in the VMD [16]. Besides, to avoid the failure of the VMD for non-stationary time-domain signals with chirp modes, McNeill [18] proposed the use of an optimized objective function with constraints on short-time narrow-band modes and Chen et al. [19] exploited a complete variational framework to generalize the VMD. The empirical wavelet transform (EWT) employs an adaptive wavelet filter bank based on segments of Fourier spectra [20]. The workability of the EWT has been improved in Refs. [21–23] to eliminate its requirement for a high signal-to-noise ratio in a signal to be decomposed. The EWT has been enhanced by using Fourier-Bessel series expansion method to improve time-frequency representations (TFRs) of non-stationary signals [24]. However, transition phases between filter functions in a wavelet filter bank in the EWT can lead to the model mixing problem for signals with closely-spaced modes. Besides, a trivial component problem can occur, where the first decomposed component by the EWT corresponds to a trivial residual. Due to the inclusion of the trivial decomposed component, the number of predefined components in a signal to be decomposed is hard to determine. Fourier decomposition method (FDM) [25] is an adaptive non-stationary, non-linear signal decomposition method that decomposes a zero-mean signal into a set of Fourier intrinsic band functions (FIBFs) based on Fourier theory and Hilbert transform. Several limitations of the FDM have been identified. To obtain a FIBF, two frequency scan techniques are developed. One is called the low-to-high (LTH) technique and the other is the high-to-low (HTL) technique. The LTH and HTL techniques recursively estimate FIBFs by using forward manner and backward manner, respectively. However, decomposition results by the FDM with the two frequency scan techniques, i.e., FDM-HTL and FDM-LTH, can be inconsistent and one cannot determine which decomposition results are correct. Further, the two frequency scan techniques are both iterative and require long computation times for FDM. Recently, uses of discrete cosine transforms (DCTs), non-causal infinite impulse response filters and finite impulse response filters have been introduced to generalize the FDM [26,27]. For example, the DCT based FDM (FDM-DCT) uses DCTs to obtain several analytic FIBFs with predefined cut-off frequencies, and it improves the accuracy of TFRs by the FDM [27].

In this work, the EWT and the FDM are briefly reviewed. The segmentation technique and construction of a wavelet filter bank in the EWT are described, and the construction of FIBFs and the two frequency scan techniques for the FDM are described. A new adaptive signal decomposition method, called the empirical Fourier decomposition (EFD), is proposed to solve the aforementioned problems of the EWT and FDM. The main contributions of the EFD are: (1) it can simultaneously solve the trivial component problem and mode mixing problem that occur to decomposition results by the EWT, and (2) it can solve the inconsistency problem in decomposition results by FDM. The two contributions of the proposed EFD are significant and they derive from the combination of an improved segmentation technique and a zero-phase filter bank. Numerical investigations are conducted to study the accuracy of decomposition results by the EFD for two non-stationary signals and two signals with closely-spaced modes by comparing with decomposition results by the EMD, VMD, EWT and FDM. In addition, the accuracy of TFRs and computational efficiency of the EFD are compared with those associated with the other methods. An experimental validation is also conducted to study the effectiveness of the EFD for experimentally measured signals with closely-spaced modes.

The remnant of the paper is arranged as follows. In Section 2, the EWT and FDM are briefly reviewed. In Section 3, the proposed EFD is described. In Section 4, the numerical investigations are presented. In Section 5, the experimental investigation is presented. Conclusions and some discussions on future works are presented in Section 6.

### 2. Reviews of EWT and FDM

#### 2.1. EWT

The EWT employs an adaptive wavelet transform algorithm based on segments of Fourier spectra [20]. The two most important steps of the EWT are: (1) use of an adaptive segmentation technique to divide Fourier spectrum of a signal to be decomposed and (2) construction of a wavelet filter bank [28]. Assume that the spectrum is defined on a normalized frequency range  $[-\pi, \pi]$ . The segmentation technique and wavelet filter bank for the spectrum in the frequency range  $[0, \pi]$  are described below, and those for the spectrum in the frequency range  $[-\pi, 0]$  can be deduced based on Hermitian symmetry of Fourier spectrum in the normalized

frequency range  $[-\pi, \pi]$ .

One segmentation technique for the EWT is the local maxima technique [20], in which the spectrum in  $[0,\pi]$  is divided into N contiguous frequency segments. Each segment is denoted by  $S_n = [\omega_{n-1},\omega_n]$  with  $n \in [1,N], \omega_0 = 0$  and  $\omega_N = \pi$ . To determine values of  $\omega_n$ , the first N-1 largest local maxima of the spectrum magnitude are identified. The frequencies that uniquely correspond to the identified maxima are re-indexed in descending order and denoted by  $[\Omega_1,\Omega_2,...\Omega_{N-1}]$  such that  $\Omega_1 < \Omega_2 < ... < \Omega_{N-1}$ ; in addition,  $\Omega_0 = 0$  is defined. The value of  $\omega_n$  is expressed by

$$\omega_n = \frac{\Omega_{n-1} + \Omega_n}{2}, \ n \in [1, N-1]$$
 (1)

which concludes the local maxima technique. As an alternative to the local maxima technique, the lowest minima technique [29] was developed for the EWT: the spectrum division and frequency reindexing procedures, which are the same as those in the local maxima technique, are first carried out. Then the minimum of the spectrum magnitude in the frequency range  $[\Omega_{n-1}, \Omega_n]$  is identified and the value of  $\omega_n$  is determined by

$$\omega_n = \underset{\omega}{\arg\min} X_n(\omega) \tag{2}$$

where  $X_n(\omega)$  denotes spectrum magnitudes between in  $[\Omega_{n-1},\Omega_n]$  and  $\operatorname{argmin}(\cdot)$  denotes argument of the minimum, respectively, which concludes the lowest minima technique.

The wavelet filter bank is then constructed, and it consists of an empirical scaling function  $\widehat{\phi}_1(\omega)$  and a series of empirical wavelet functions  $\widehat{\psi}_n(\omega)$ , which are expressed by

$$\widehat{\phi}_{1}(\omega) = \begin{cases} 1 & \text{if } |\omega| \leqslant \omega_{1} - \tau_{1} \\ \cos\left[\frac{\pi}{2}\beta\left(\frac{1}{2\tau_{1}}(\tau_{1} + |\omega| - \omega_{1})\right)\right] & \text{if } \omega_{1} - \tau_{1} \leqslant |\omega| \leqslant \omega_{1} + \tau_{1} \\ 0 & \text{otherwise} \end{cases}$$
(3)

and

$$\widehat{\psi}_{n}(\omega) = \begin{cases} 1 & \text{if } \omega_{n} + \tau_{n} \leq |\omega| \leq \omega_{n+1} - \tau_{n+1} \\ \cos\left[\frac{\pi}{2}\beta\left(\frac{1}{2\tau_{n+1}}(\tau_{n+1} + |\omega| - \omega_{n+1})\right)\right] & \text{if } \omega_{n+1} - \tau_{n+1} \leq |\omega| \leq \omega_{n+1} + \tau_{n+1} \\ \sin\left[\frac{\pi}{2}\beta\left(\frac{1}{2\tau_{n}}(\tau_{n} + |\omega| - \omega_{n})\right)\right] & \text{if } \omega_{n} - \tau_{n} \leq |\omega| \leq \omega_{n} + \tau_{n} \\ 0 & \text{otherwise} \end{cases}$$

in which respectively,  $\hat{\cdot}$  denotes Fourier transform of a function,  $\omega$  the circular frequency,  $\beta$  an arbitrary function and  $\tau_n$  a parameter that determines the size of the transition phase [20] associated with the *n*-th and (n+1)-th segments; the transition phase ranges in  $[\omega_n - \tau_n, \omega_n + \tau_n]$ . One of the most used forms of  $\beta$  in Eqs. (3) and (4) with a variable x is [28]:

$$\beta(x) = \begin{cases} 0 & \text{if } x \le 0\\ x^4 (35 - 84x + 70x^2 - 20x^3) & \text{if } 0 < x < 1\\ 1 & \text{if } x \ge 1 \end{cases}$$
 (5)

The parameter  $\tau_n$  is calculated by

$$\tau_n = \gamma \omega_n$$
 (6)

where  $\gamma$  is a sufficiently small parameter, so that it prevents overlapping between boundaries of non-zero  $\widehat{\phi}_1(\omega)$  and  $\widehat{\psi}_n(\omega)$ . A criterion for an acceptable value of  $\gamma$  is:

$$\gamma < \min_{n} \left( \frac{\omega_{n+1} - \omega_n}{\omega_{n+1} + \omega_n} \right) \tag{7}$$

for all n values, and its value can be determined by

$$\gamma = \left(\frac{R-1}{R}\right) \min_{n} \left(\frac{\omega_{n+1} - \omega_{n}}{\omega_{n+1} + \omega_{n}}\right) \tag{8}$$

where R is the number of discrete data in the signal to be decomposed. The determination of  $\widehat{\phi}_1(\omega)$  and  $\widehat{\psi}_n(\omega)$  concludes the construction of the wavelet filter bank. Graphical illustrations of  $\widehat{\phi}_1(\omega)$  and  $\widehat{\psi}_n(\omega)$  are shown in Fig. 1(a) and (b), respectively.

After applying a segmentation technique and constructing a filter bank, a decomposed signal can be reconstructed as

$$\widetilde{f}(t) = W_f^{\varepsilon}(0, t) * \phi_1(t) + \sum_{n=1}^{N-1} W_f^{\varepsilon}(n, t) * \psi_n(t)$$

$$\tag{9}$$

where the asterisk \* denotes the convolution of two functions,  $W_f^{\epsilon}(0,t)$  and  $W_f^{\epsilon}(n,t)$  are called the approximation coefficient function and detail coefficient function, respectively. The function  $W_f^{\epsilon}(0,t)$  is expressed by

$$W_f^{\varepsilon}(0,t) = F^{-1}(\widehat{f}(\omega)\widehat{\phi}_1(\omega)) = \int_{-\omega_1 - \tau_1}^{\omega_1 + \tau_1} f(\tau)\overline{\phi_1(\tau - t)} d\tau$$
(10)

where the overbar denotes complex conjugation and  $F^{-1}$  denotes the inverse Fourier transform of a function. Note that  $F^{-1}(\widehat{\phi}_1(\omega)) = \phi_1(t)$  and  $F^{-1}(\widehat{\psi}_n(\omega)) = \psi_n(t)$ . The function  $W_f^\varepsilon(n,t)$  is expressed by

$$W_{f}^{\varepsilon}(n,t) = F^{-1}(\widehat{f}(\omega)\widehat{\psi}_{n}(\omega)) = \int_{-\omega_{n+1}-\tau_{n+1}}^{\tau_{n}-\omega_{n}} f(\tau)\overline{\psi_{n}(\tau-t)}d\tau + \int_{\omega_{n}-\tau_{n}}^{\omega_{n+1}+\tau_{n+1}} f(\tau)\overline{\psi_{n}(\tau-t)}d\tau$$

$$\tag{11}$$

Resulting decomposed components of the signal can be expressed by

$$f_0(t) = W_{\ell}^{\epsilon}(0, t) *\phi_1(t)$$
 (12)

and

$$f_n(t) = W_\ell^e(n, t) * \psi_n(t)$$
 (13)

A step-by-step description of the EWT for a signal f(t) is provided as follows.

- **Step 1.** Obtain a Fourier spectrum of f(t) using Fourier transform.
- **Step 2.** Segment the spectrum in Step 1 using a segmentation technique, such as the local maxima technique and lowest minimum technique.
  - Step 3. Construct a wavelet filter bank based on the frequency segments in Step 2.
  - Step 4. Express approximation and detail coefficient functions based on the wavelet filter bank in Step 3.
  - **Step 5.** Decompose f(t) and reconstruct it using Eq. (9).

The EWT can yield accurate decomposition results when f(t) does not have closely-spaced modes. However, when f(t) has closely-spaced modes, a mode mixing problem can occur due to the transition phase.

#### 2.2. FDM

Assume that f(u) is zero-mean, discrete, and a length-limited signal within one period U, which is an even integer; the fundamental frequency of f(u) can be expressed by

$$\varphi_0 = \frac{2\pi}{U} \tag{14}$$

In the FDM, f(u) is approximated by a summation of K orthogonal FIBFs  $g_k(u)$  [25]:

$$f(u) = \sum_{k=1}^{K} g_k(u) \tag{15}$$

Based on Eq. (15), the analytical signal of f(u) can be expressed by [30]

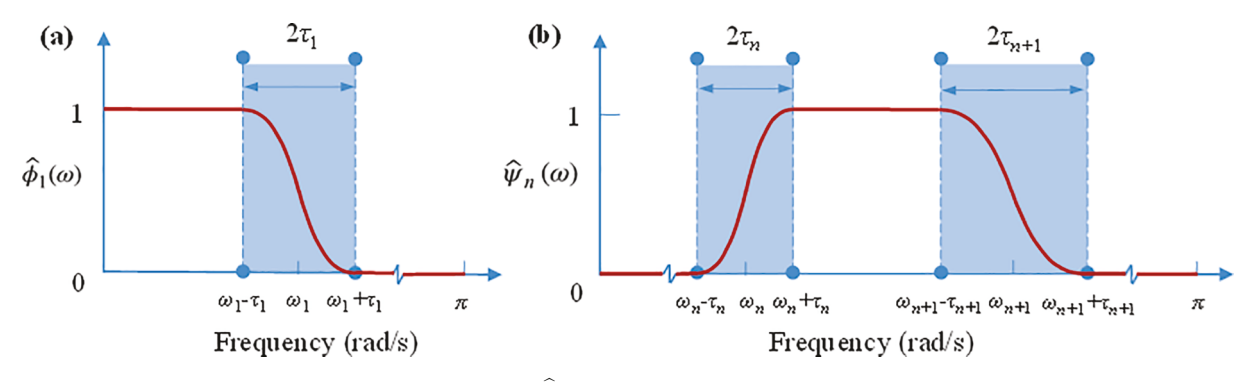


**Fig. 1.** Graphical illustrations of (a)  $\widehat{\phi}_1(\omega)$  and (b)  $\widehat{\psi}_n(\omega)$ . Shaded parts are transition phases.

$$z(u) = f(u) + jH(f(u)) = \sum_{k=1}^{K} [g_k(u) + jH(g_k(u))] = \sum_{k=1}^{K} z_k(u)$$
(16)

where  $H(\cdot)$  denotes Hilbert transform of a function,  $j = \sqrt{-1}$ , and  $z_k(u) = g_k(u) + jH(g_k(u))$ . The term  $z_k(u)$  can be considered as the analytical signal corresponding to  $g_k(u)$ . Note that z(u) can be expressed as Fourier series:

$$z(u) = \sum_{m=1}^{U/2-1} a_m e^{jm\varphi_0 u}$$
 (17)

where

$$a_m = \frac{2}{U} \sum_{u=0}^{U-1} f(u) e^{-jm\varphi_0 u}$$
 (18)

and values of  $a_m$  can be estimated using discrete Fourier transform.

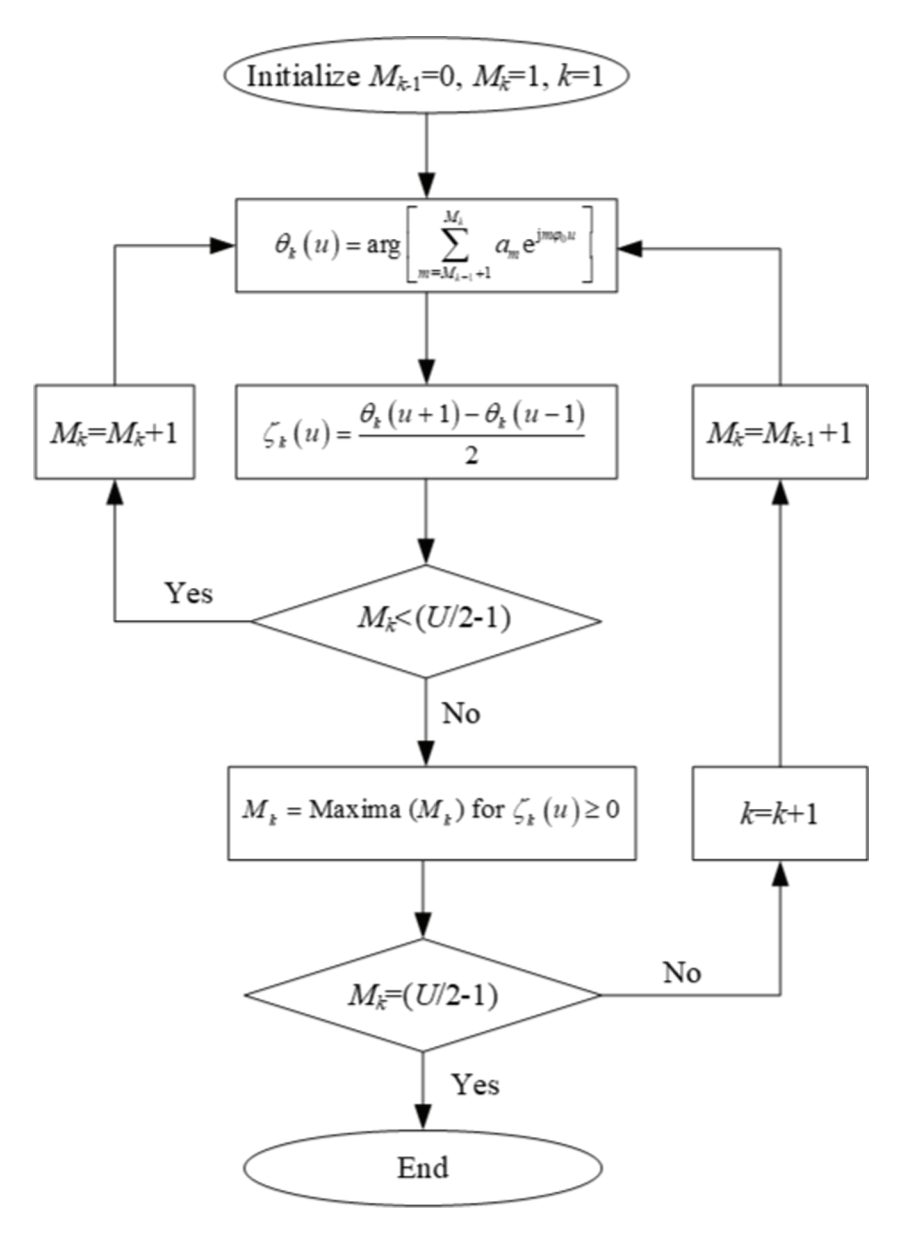


Fig. 2. Flowchart of the LTH technique.

The analytical signal  $z_k(u)$  can be considered as a filtered signal by Hilbert transform filter [31], which is the counterpart of a filter in the wavelet filter bank in the EWT, and  $z_k(u)$  can be further expressed by

$$z_k(u) = \sum_{m=M_{k-1}+1}^{M_k} a_m e^{jm\varphi_0 u}$$
 (19)

where  $M_k$  ranges from 1 to (U/2-1) with  $M_0=0$ . Determination of values of  $M_k$  is similar to the segmentation in the EWT. In the FDM, two frequency scan techniques have been proposed to determine the values of  $M_k$  in Eq. (19), including the LTH technique and the HTL technique [25]. Flowcharts of the LTH and HTL techniques are shown in Figs. 2 and 3, respectively. In the LTH technique, K values of  $M_k$  are searched in a forward manner so that  $M_1 < M_2 < \ldots < M_k \ldots < M_k$ , with which

$$z_{1}(u) = \sum_{m=M_{0}+1}^{M_{1}} a_{m} e^{jm\varphi_{0}u}$$

$$z_{2}(u) = \sum_{m=M_{1}+1}^{M_{2}} a_{m} e^{jm\varphi_{0}u}$$
(20)

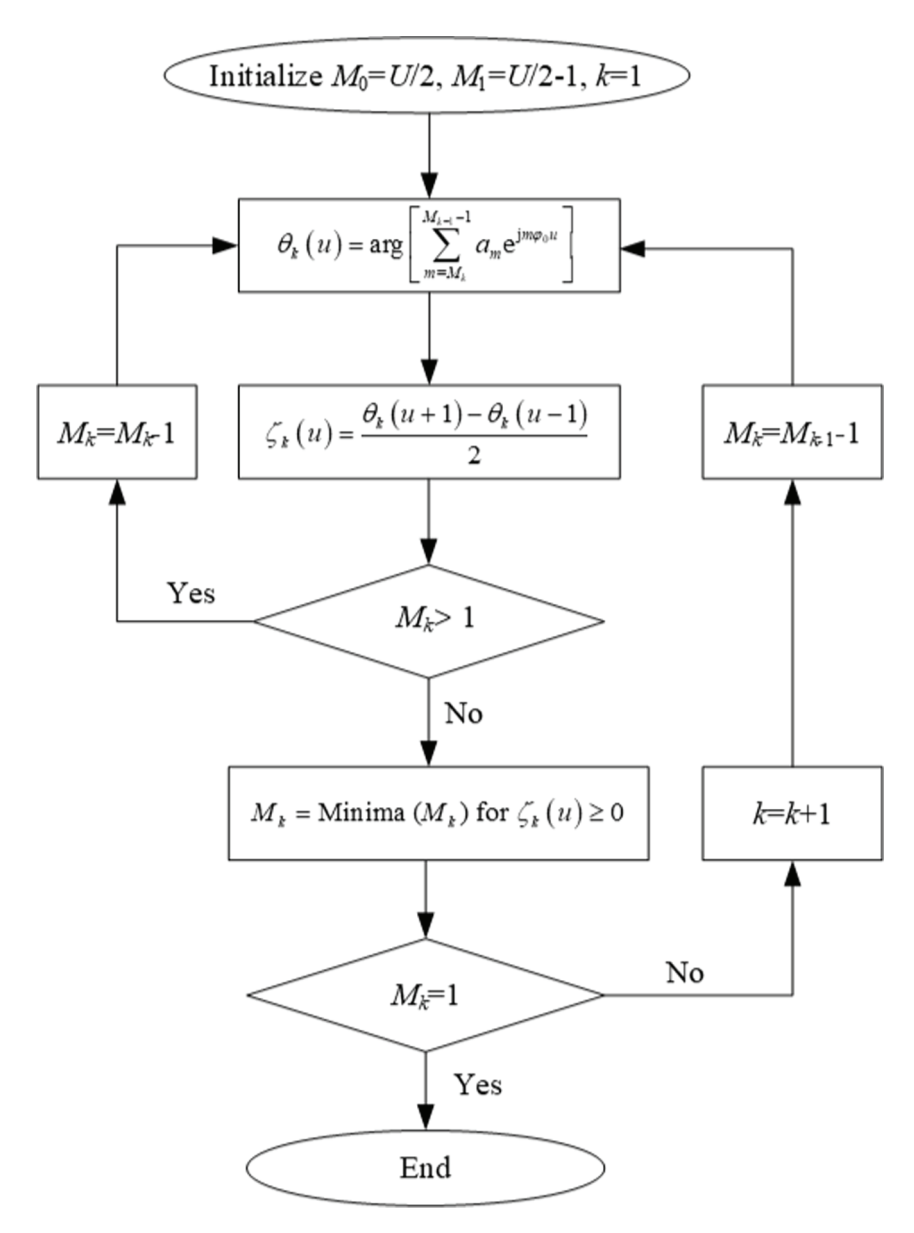


Fig. 3. Flowchart of the HTL technique.

W. Zhou et al.

$$z_K(u) = \sum_{m=M_0, j=1}^{M_K} a_m e^{jm\varphi_0 u}$$

where  $M_0=0$  and  $M_K=U/2-1$ . The signal  $z_k(u)$  can further be expressed by

$$z_k(u) = A_k(u)e^{i\theta_k(u)} \tag{21}$$

where

$$A_k(u) = \left\| \sum_{m=M_{k-1}+1}^{M_k} a_m e^{jm\varphi_0 u} \right\|_2 \tag{22}$$

and

$$\theta_k(u) = \arg \left[ \sum_{m=M_{k-1}+1}^{M_k} a_m e^{jm\varphi_0 u} \right]$$
(23)

denote instantaneous amplitude and phase of  $z_k(u)$ , respectively, in which  $\|\cdot\|_2$  and  $\arg(\cdot)$  calculate Euclidean norm and argument of a complex quantity, respectively. The FIBFs  $g_k(u)$  can be obtained by

$$g_k(u) = \text{Re}\left[A_k(u)e^{j\theta_k(u)}\right] \tag{24}$$

where  $Re(\cdot)$  is the real part of a function. In the HTL technique, K values of  $M_k$  are searched in a backward manner so that  $M_K < ... M_k < M_{k-1} < ... < M_1$ , with which

$$z_{1}(u) = \sum_{m=M_{1}}^{M_{0}-1} a_{m} e^{jm\varphi_{0}u}$$

$$z_{2}(u) = \sum_{m=M_{2}}^{M_{1}-1} a_{m} e^{jm\varphi_{0}u}$$
(25)

$$\vdots$$

$$z_K(u) = \sum_{m=M_K}^{M_{K-1}-1} a_m e^{jm\varphi_0 u}$$

where  $M_0 = U/2$  and  $M_K = 1$ .

A step-by-step description of the FDM for f(u) is as follows.

**Step 1.** Obtain a Fourier spectrum of f(u) using Fourier transform.

**Step 2.** Express z(u) using the spectrum of f(u) obtained in Step 1.

**Step 3.** Obtain  $K z_k(u)$  using the LTH or HTL technique.

**Step 4.** Obtain FIBFs  $g_k(u)$  from the real part of  $z_k(u)$  obtained in Step 3.

**Step 5.** Reconstruct f(u) as a summation of FIBFs  $g_k(u)$  obtained in Step 4.

An issue of the FDM is that its decomposition results using the LTH technique can be inconsistent with that using the HTL technique, and the issue will be verified in the numerical investigation in Section 4.

# 3. EFD

Similar to the EWT and FDM, the EFD consists of two critical steps: an improved segmentation technique and construction of a zero-phase filter bank. In the EFD, Fourier spectrum of a signal to be decomposed is defined on a normalized frequency range  $[-\pi,\pi]$ , and the improved segmentation technique and construction of a zero-phase filter bank for the spectrum in the frequency range  $[0,\pi]$  are described below.

#### 3.1. Improved segmentation technique

The improved segmentation technique is proposed based on the lowest minima technique [29] described in Section 2.1. In the improved segmentation technique,  $[0,\pi]$  is divided into N contiguous frequency segments. Unlike the local maxima and lowest minima techniques,  $\omega_0$  and  $\omega_N$  are not necessarily equal to 0 and  $\pi$ , respectively, and their values are determined in an adaptative sorting process. In the sorting process, Fourier spectrum magnitudes at  $\omega=0$  and  $\omega=\pi$  and their local maxima are identified and extracted to a series. All magnitudes in the series are sorted in descending order. Frequencies corresponding to the first N largest values in the sorted series are denoted by  $[\Omega_1,\Omega_2,...\Omega_N]$ . In addition,  $\Omega_0=0$  and  $\Omega_{N+1}=\pi$  are defined. Boundaries of each segment are determined by

$$\omega_n = \begin{cases} \underset{\omega}{\operatorname{argmin}} \check{X}_n(\omega) & \text{if } 0 \leq n \leq N \text{ and } \Omega_n \neq \Omega_{n+1} \\ \Omega_n & \text{if } 0 \leq n \leq N \text{ and } \Omega_n = \Omega_{n+1} \end{cases}$$
(26)

where  $\check{X}_n(\omega)$  denotes the Fourier spectrum magnitudes between  $\Omega_n$  and  $\Omega_{n+1}$ , which concludes the improved segmentation technique.

### 3.2. Construction of a zero-phase filter bank

Both the EWT and FDM consist of a step of constructing a filter bank. In the EWT, a wavelet filter bank is formed by the empirical scaling function and wavelet functions. In the FDM, Hilbert transform filter bank is constructed based on Fourier spectrum of the analytical signal associated with a signal to be decomposed. In the EFD, a zero-phase filter bank is constructed based on frequency segments obtained by the improved segmentation technique. In each frequency segment, a zero-phase filter [32] is a band-pass filter with  $\omega_{n-1}$  and  $\omega_n$  serving as its cut-off frequencies and it has not transition phases. Hence, the zero-phase filter retains the major Fourier spectrum component in the segment and all other Fourier spectrum components beyond the segment are excluded.

Fourier transform of a signal to be decomposed f(t) is expressed as

$$\widehat{f}(\omega) = \int_{-\infty}^{\infty} f(t) e^{-j\omega t} dt$$
(27)

a zero-phase filter bank can be constructed by  $\widehat{\mu}_n(\omega)$ :

$$\widehat{\mu}_n(\omega) = \begin{cases} 1 & \text{if } \omega_{n-1} \leq |\omega| \leq \omega_n \\ 0 & \text{otherwise} \end{cases}$$
 (28)

where  $1 \le n \le N$  and values of  $\omega_n$  are determined by Eq. (26). A graphical illustration of the zero-phase filter bank is shown in Fig. 4. Filtered signals that correspond to  $\widehat{\mu}_n(\omega)$  are calculated by

$$\widehat{f}_{n}(\omega) = \widehat{\mu}_{n}(\omega)\widehat{f}(\omega) = \begin{cases} \widehat{f}(\omega) & \text{if } \omega_{n-1} \leq |\omega| \leq \omega_{n} \\ 0 & \text{otherwise} \end{cases}$$
(29)

Decomposed components in the time domain can be obtained using the inverse Fourier transform:

$$f_n(t) = F^{-1} \Big[ \widehat{f_n}(\omega) \Big] = \int_{-\infty}^{\infty} \widehat{f_n}(\omega) e^{j\omega t} d\omega = \int_{-\omega_n}^{-\omega_{n-1}} \widehat{f}(\omega) e^{j\omega t} d\omega + \int_{\omega_{n-1}}^{\omega_n} \widehat{f}(\omega) e^{j\omega t} d\omega$$
(30)

The reconstructed signal is calculated as a summation of all decomposed components:

$$\widetilde{f}(t) = \sum_{n=1}^{N} f_n(t) \tag{31}$$

A flowchart of the EFD is shown in Fig. 5 and a step-by-step description of the EFD is provided as follows.

- **Step 1.** Obtain Fourier spectrum of a signal to be decomposed f(t) using Fourier transform.
- **Step 2.** Determine boundaries of segment  $\omega_n$  using the improved segmentation technique based on Fourier spectrum obtained in Step 1.
  - **Step 3.** Construct a zero-phase filter bank  $\widehat{\mu}_n(\omega)$  based on  $\omega_n$  obtained in Step 2.
  - **Step 4.** Obtain filtered signals  $\widehat{f}_n(\omega)$  in the frequency domain using  $\widehat{\mu}_n(\omega)$  obtained in Step 3.
  - **Step 5.** Obtain decomposed components  $f_n(t)$  in the time-domain using inverse Fourier transforms of  $\widehat{f}_n(\omega)$  obtained in Step 4.

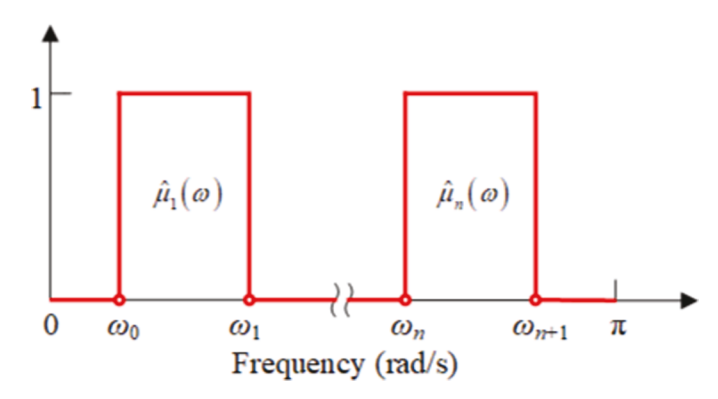


Fig. 4. Graphical illustration of an ideal filter bank of the EFD.

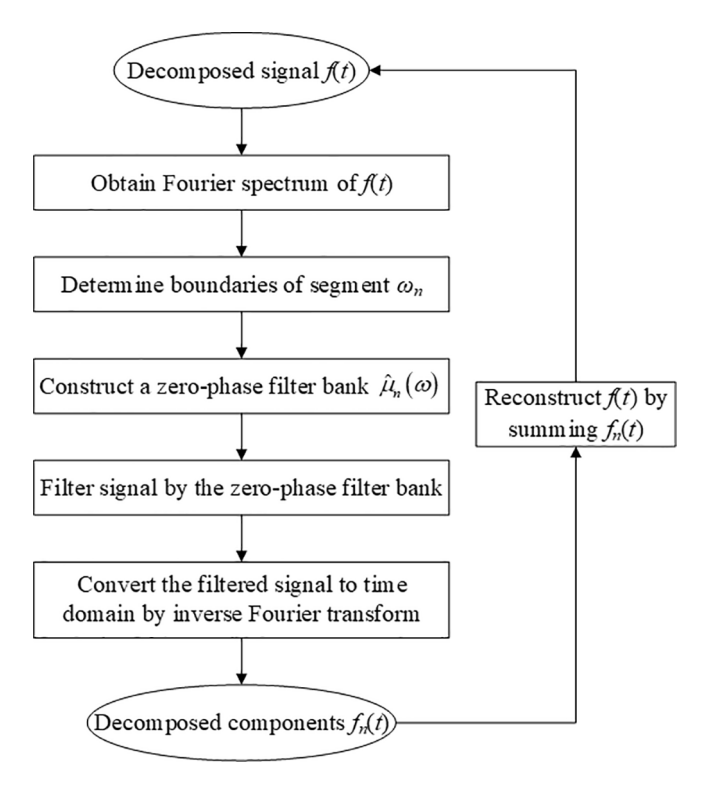


Fig. 5. Flowchart of the EFD.

# 4. Numerical investigation

In this section, the effectiveness of the lowest minima and improved segmentation techniques are compared based on two typical signals that have multiple modes, denoted by  $f_{\text{Sig1}}(t)$  and  $f_{\text{Sig2}}(t)$ . Decomposition accuracy of the proposed EFD method is compared with those of the EWT [20], FDM [25], VMD [16] and EMD [7] methods for two typical non-stationary time-domain signals  $f_{\text{Sig3}}(t)$  and  $f_{\text{Sig4}}(t)$ , and two stationary time-domain signals  $f_{\text{Sig5}}(t)$  and  $f_{\text{Sig6}}(t)$ , with closely-spaced modes. For the EFD, EWT and VMD, the numbers of decomposed components are listed in Table 1.

# 4.1. Comparison of segmentation techniques

The signals  $f_{\text{Sig1}}(t)$  and  $f_{\text{Sig2}}(t)$  are expressed by

$$f_{\text{Sig1}}(t) = 6t + \cos(24\pi t) + \cos(50\pi t) + \delta(t)$$
 (32)

and

$$f_{\text{Sig2}}(t) = \cos(20\pi t) + \cos(24\pi t) + \cos(50\pi t) + \delta(t)$$
 (33)

where  $\delta(t)$  is a random white-noise such that  $f_{\text{Sig1}}(t)$  and  $f_{\text{Sig2}}(t)$  have signal-to-noise-ratios of 10 dB. Segmentation results of  $f_{\text{Sig1}}(t)$  by the lowest minima and improved segmentation techniques are shown in Fig. 6: the first two segments by the two techniques are the

Table 1
Numbers of components to be decomposed for.

Signal	Decomposition method				
	EFD	EWT	VMD		
$f_{\mathrm{Sig1}}(t)$	3	3	-		
$f_{\mathrm{Sig2}}(t)$ $f_{\mathrm{Sig3}}(t)$ $f_{\mathrm{Sig4}}(t)$	3	4	-		
$f_{ m Sig3}(t)$	2	2	2		
$f_{\mathrm{Sig4}}(t)$	3	3	3		
$f_{\mathrm{Sig5}}(t)$	3	4	3		
$f_{\mathrm{Sig6}}(t)$	2	3	2		

same, but the last segment in the improved segmentation technique has a narrower frequency range than that by the lowest minima technique. Therefore, the improved segmentation technique alleviates the effect of noise on the decomposed component associated with the last segment. Segmentation results of  $f_{\text{Sig2}}(t)$  by the lowest minima and improved segmentation techniques are shown in Fig. 7. The first segment by the lowest minima technique, shown in Fig. 7(a), can be considered trivial as it does not contain a meaningful Fourier spectrum component and its associated decomposed component consists of noise only. On the other hand, the trivial segment is excluded in segmentation results by the improved segmentation technique, shown in Fig. 7(b), and its first resulting segment contains a meaningful Fourier spectrum component. Hence, the improved segmentation technique solves the trivial component problem in the EWT. Segmentation results of the last segments by the two techniques are similar to those of  $f_{\text{Sig1}}(t)$ : the decomposed component associated with the improved segmentation technique has a lower level of noise than that by the lowest minima technique.

# 4.2. Non-stationary multimode signals

The non-stationary multimode signal  $f_{Sig3}(t)$  is expressed by

$$\begin{cases} f_{\text{Sig3C1}}(t) &= \frac{1}{1.2 + \cos(2\pi t)} \\ f_{\text{Sig3C2}}(t) &= \frac{\cos(32\pi t + 0.2\cos(64\pi t))}{1.5 + \sin(2\pi t)} \\ f_{\text{Sig3}}(t) &= f_{\text{Sig3C1}}(t) + f_{\text{Sig3C2}}(t) \end{cases}$$
(34)

The signal  $f_{\text{Sig3}}(t)$  consists of two modes  $f_{\text{Sig3C1}}$  and  $f_{\text{Sig3C2}}$  in Eq. (34), which are shown in Fig. 8(a) and (b) [33], and  $f_{\text{Sig3}}(t)$  is similar to the expression of a solution to Duffing equation [7]. The signal  $f_{\text{Sig3}}(t)$  is sampled at a frequency of 1000 Hz for one second and shown in Fig. 8(c).

Decomposition results of  $f_{Sig3}(t)$  by the EFD, EWT, FDM-LTH, FDM-HTL, VMD, and EMD are shown in Fig. 9. Root-mean-square errors (RMSEs) between the decomposition results and analytical ones are calculated by

RMSE = 
$$\sqrt{\frac{1}{R} \sum_{r=1}^{R} |y_r - \widetilde{y}_r|^2}$$
 (35)

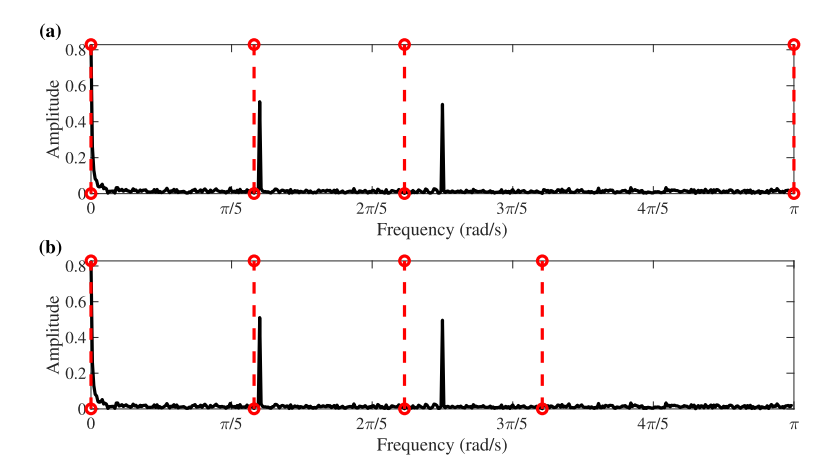
where  $y_r$  is the analytical component at the r-th discrete instant, and  $\tilde{y}_r$  is the corresponding component at the r-th discrete instant obtained by a decomposition method. RMSEs associated with the aforementioned decomposition methods are calculated and listed in Table 2. For  $f_{\text{Sig3C1}}$ , it can be seen that the RMSE associated with the EMD is the smallest and that associated with the EFD is the second smallest. While the RMSEs associated with the EWT, VMD and FDM-LTH are relatively small, that associated with the FDM-HTL is large. For  $f_{\text{Sig3C2}}$ , results similar to  $f_{\text{Sig3C1}}$  can be observed: RMSEs associated with the EMD and EFD are the smallest, and the RMSEs of the EWT, VMD and FDM-LTH are relatively small. In addition, the RMSE associated with the FDM-HTL is also large. It is indicated that the EFD accurately decomposes the non-stationary multimode signal. The inconsistency of decomposition results by the FDM-LTH and FDM-HTL is verified.

Another non-stationary multimode signal  $f_{Sig4}(t)$  is expressed by [33]

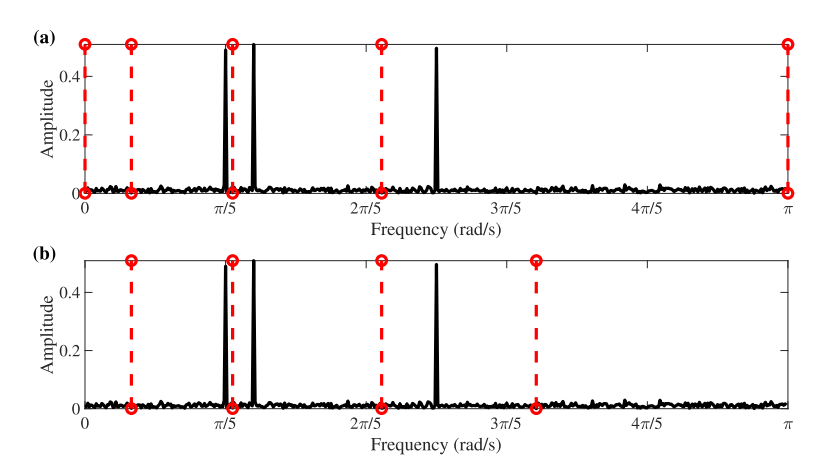
$$\begin{cases} f_{\text{Sig4C1}}(t) &= 6t \\ f_{\text{Sig4C2}}(t) &= \cos(8\pi t) \\ f_{\text{Sig4C3}}(t) &= 0.5\cos(40\pi t) \\ f_{\text{Sig4}}(t) &= f_{\text{Sig4C1}}(t) + f_{\text{Sig4C2}}(t) + f_{\text{Sig4C3}}(t) \end{cases}$$
(36)

The signal  $f_{\text{Sig4C1}}$  consists of three modes: one mode  $f_{\text{Sig4C1}}$  with a monotonically increasing amplitude as shown in Fig. 10(a) and two modes  $f_{\text{Sig4C2}}$  and  $f_{\text{Sig4C3}}$  with sinusoidal amplitudes as shown in Fig. 10(b) and (c), respectively. The signal  $f_{\text{Sig4}}(t)$  is sampled at a frequency of 1000 Hz for one second and shown in Fig. 10(d).

The EFD, EWT, FDM-LTH, FDM-HTL, VMD and EMD are employed to decompose the sampled  $f_{\rm Sig4}(t)$ . Their results are compared with the analytical ones as shown in Fig. 11 and corresponding RMSEs in Eq. (35) are calculated and listed in Table 3. For  $f_{\rm Sig4C1}$ , the RMSE associated with the EFD is the smallest, and those associated with the EWT, VMD and EMD are relatively small. RMSEs associated with the FDM-LTH and FDM-HTL are large. For  $f_{\rm Sig4C2}$ , RMSE associated with the EMD is the smallest, and those associated with the EFD and VMD are slightly larger than that associated with the EMD. The RMSEs associated with the EWT, FDM-LTH and FDM-HTL are large and that associated with the FDM is the largest. For  $f_{\rm Sig4C3}$ , the RMSE associated with the EFD is the smallest while those associated with the VMD and EMD are slightly larger than that associated with the EFD. Similar to the observations for  $f_{\rm Sig4C2}$ , the RMSEs associated with the EWT, FDM-TLH and FDM-HTL are larger than others. In theory, segmentations by the EFD and EWT are the same for  $f_{\rm Sig4}$ . However, filters in the wavelet filter bank in the EWT have transition phases that can cause mode mixing, while those in the zero-phase filter bank in the EFD do not suffer from mode mixing. Hence, the EFD can yield decomposition results with a smaller error than the EWT. It is indicated again that the EFD accurately decomposes a multimode signal. In addition, it is shown that both the FDM-LTH and FDM-HTL yields inaccurate decomposition results.



 $\textbf{Fig. 6.} \ \ \text{Segmentation results of} \ f_{Sig1}(t) \ \ \text{by (a) the lowest minima technique and (b) the improved segmentation technique.}$ 



 $\textbf{Fig. 7.} \ \ \text{Segmentation results of} \ f_{Sig2}(t) \ \ \text{by (a) the lowest minima technique and (b) the improved segmentation technique.}$ 

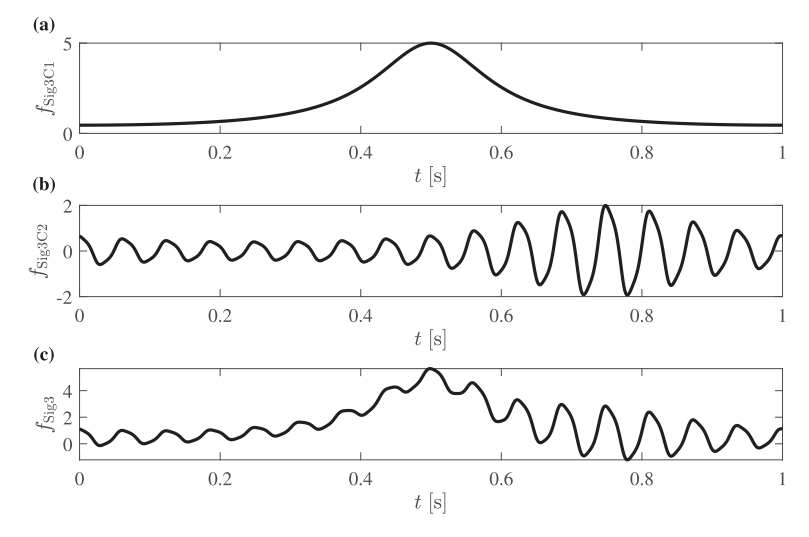


Fig. 8. (a) Modes  $f_{\text{Sig3C1}}$ , (b)  $f_{\text{Sig3C2}}$  and (c) the non-stationary signal  $f_{\text{Sig3}}(t)$  that consists of the two modes in (a) and (b) as expressed in Eq. (34).

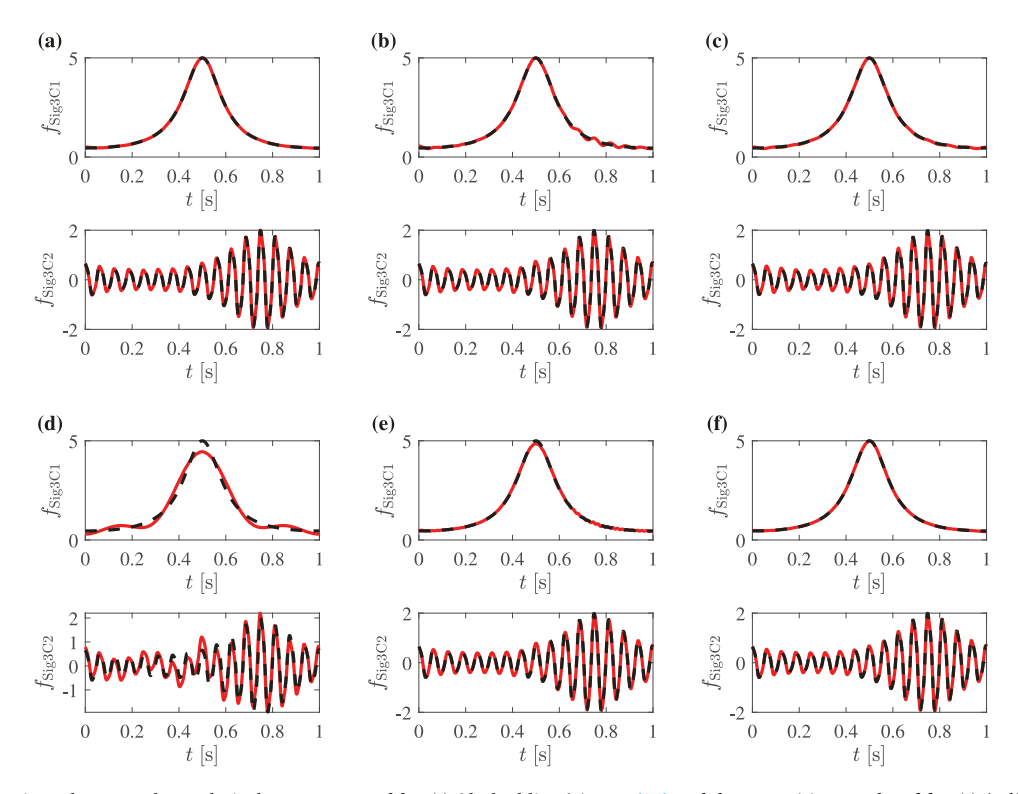


Fig. 9. Comparisons between the analytical components of  $f_{\text{Sig3}}(t)$  (dashed lines) in Eq. (34) and decomposition results of  $f_{\text{Sig3}}(t)$  (solid line) by the (a) EFD, (b) EWT, (c) FDM-LTH, (d) FDM-HTL, (e) VMD, and (f) EMD.

 $\label{eq:Table 2} \textbf{Table 2} \\ \textbf{Results of the RMSEs for } f_{\text{Sig3}}(t).$ 

Component	Decomposition method						
	EFD	EWT	FDM-LTH	FDM-HTL	VMD	EMD	
$f_{ m Sig3C1}$	$1.12\times10^{-2}$	$4.19\times10^{-2}$	$2.43\times10^{-2}$	$2.11\times10^{-1}$	$3.74\times10^{-2}$	$9.54\times10^{-3}$	
$f_{ m Sig3C2}$	$9.85\times10^{-3}$	$2.12\times10^{-2}$	$7.89\times10^{-2}$	$2.24\times10^{-1}$	$5.41\times10^{-2}$	$9.54\times10^{-3}$	

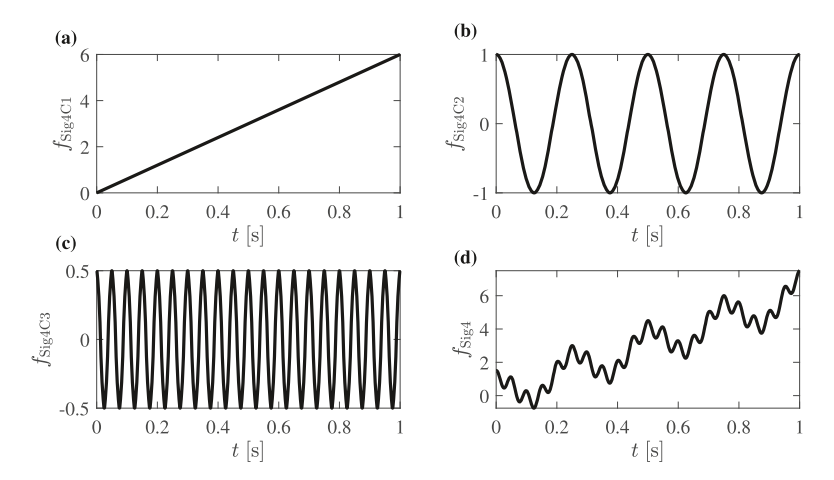


Fig. 10. (a) Modes  $f_{\text{Sig4C1}}$ , (b)  $f_{\text{Sig4C2}}$ , (c)  $f_{\text{Sig4C3}}$  and (d) the non-stationary signal  $f_{\text{Sig4}}(t)$  that consists of the three modes in (a), (b) and (c) as expressed in Eq. (36).

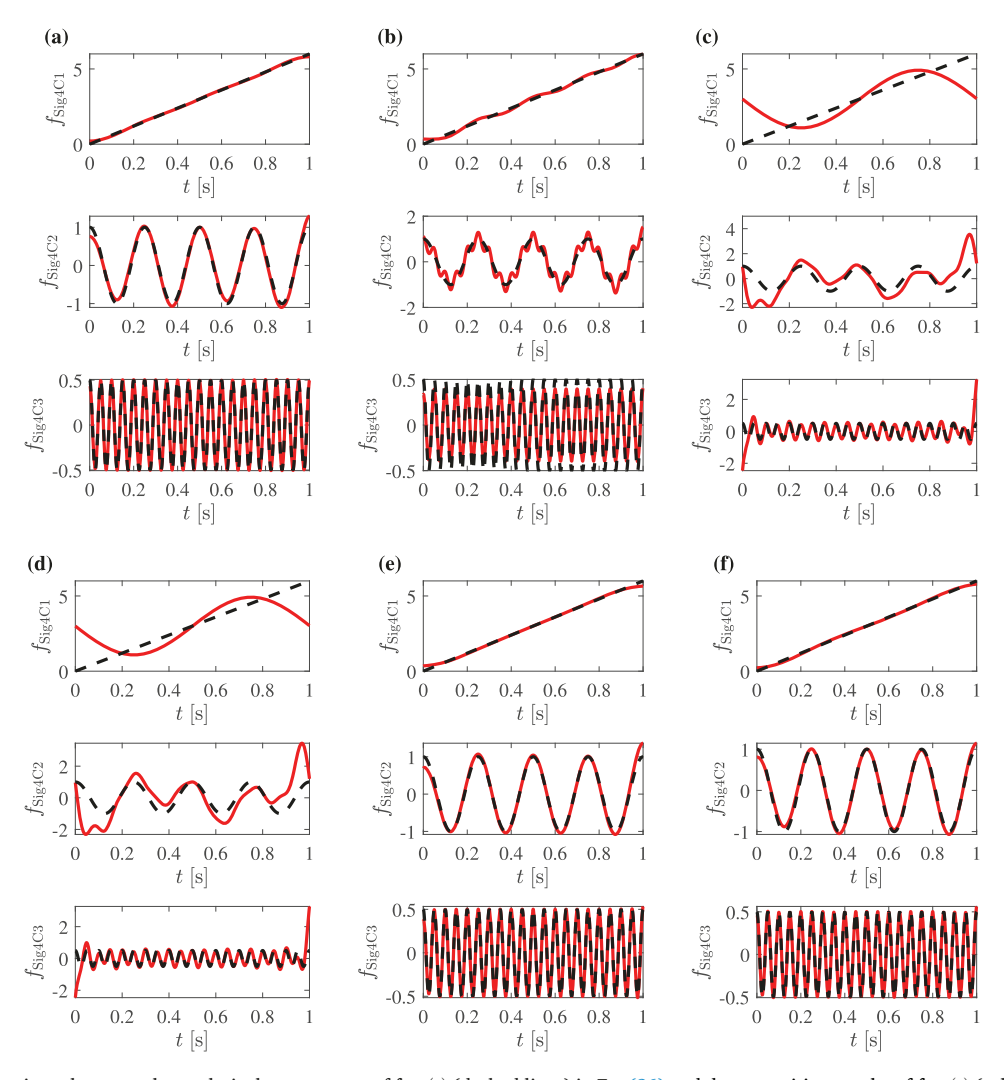


Fig. 11. Comparisons between the analytical components of  $f_{\text{Sig4}}(t)$  (dashed lines) in Eq. (36) and decomposition results of  $f_{\text{Sig4}}(t)$  (solid line) by the (a) EFD, (b) EWT, (c) FDM-LTH, (d) FDM-HTL, (e) VMD, and (f) EMD.

**Table 3** Results of the RMSEs for  $f_{Sig4}(t)$ .

Component	Decomposition method						
	EFD	EWT	FDM-LTH	FDM-HTL	VMD	EMD	
$f_{ m Sig4C1}$	$4.67\times10^{-2}$	$1.07\times10^{-1}$	$1.08\times10^{0}$	$1.08\times10^{0}$	$8.40\times10^{-2}$	$6.46\times10^{-2}$	
$f_{ m Sig4C2}$	$8.33\times10^{-2}$	$2.23\times10^{-1}$	$1.02\times 10^0$	$1.02\times10^{0}$	$9.14\times10^{-2}$	$6.38\times10^{-2}$	
$f_{ m Sig4C3}$	$7.01\times10^{-3}$	$7.43\times10^{-2}$	$3.81\times10^{-1}$	$3.98\times10^{-1}$	$9.93\times10^{-3}$	$8.10\times10^{-3}$	

#### 4.3. Closely-spaced modes

A stationary signal  $f_{\text{Sig5}}(t)$  with two closely-spaced modes is expressed by

$$\begin{cases} f_{\text{Sig5C1}}(t) &= \cos(2\pi\lambda_a t) \\ f_{\text{Sig5C2}}(t) &= \cos(2\pi\lambda_b t) \\ f_{\text{Sig5C3}}(t) &= \cos(2\pi\lambda_c t) \\ f_{\text{Sig5}}(t) &= f_{\text{Sig5C1}}(t) + f_{\text{Sig5C2}}(t) + f_{\text{Sig5C3}}(t) \end{cases}$$
(37)

where  $\lambda_a=1.1$  Hz,  $\lambda_b=1.3$  Hz and  $\lambda_c=3.1$  Hz, and it consists of a pair of closely-spaced modes shown in Figs. 12(a) and (b), and a

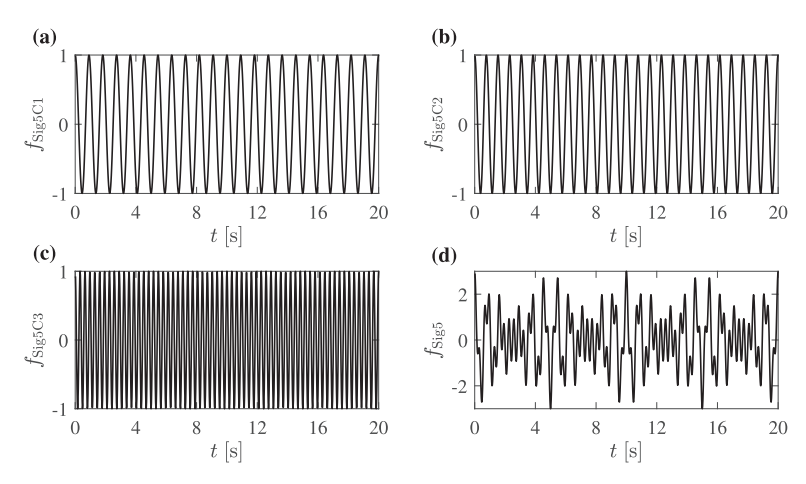
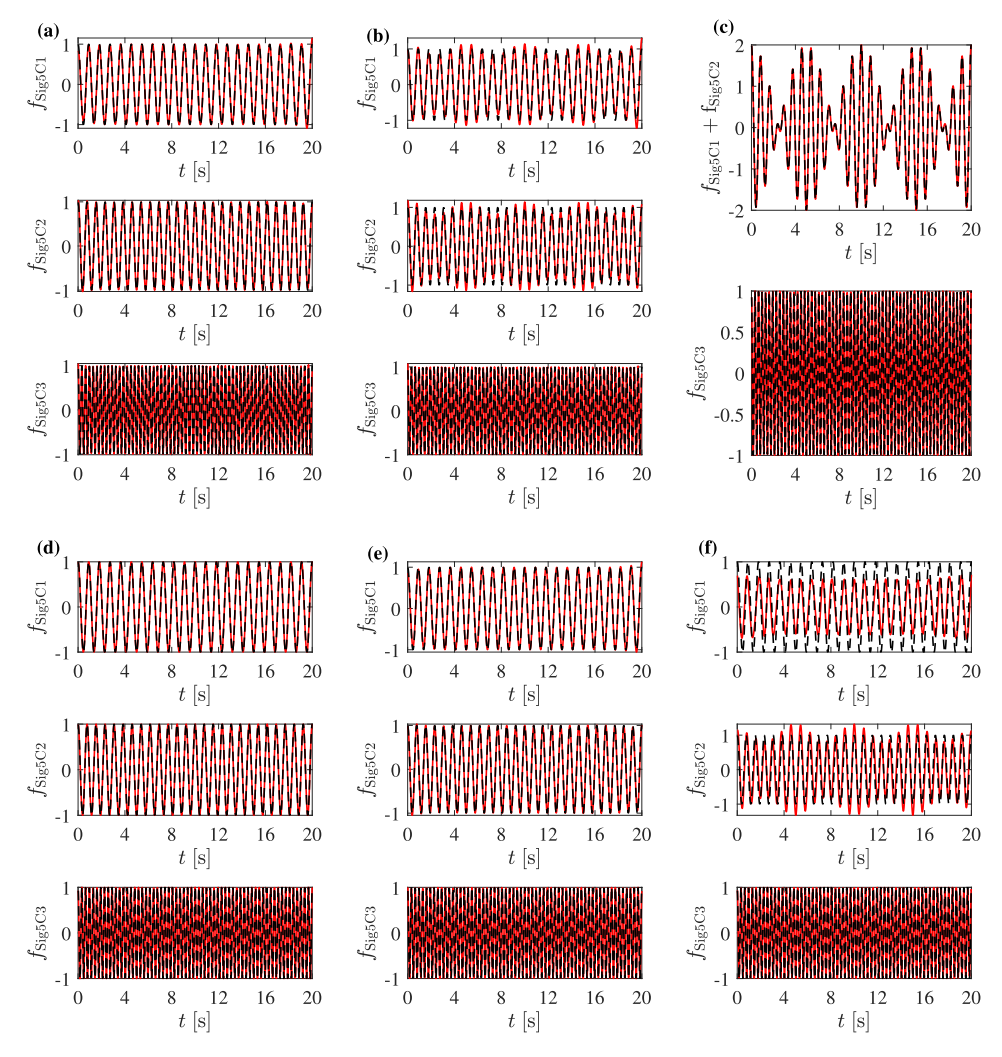


Fig. 12. (a) Modes  $f_{\text{Sig5C2}}$ , (b)  $f_{\text{Sig5C2}}$ , (c)  $f_{\text{Sig5C3}}$  and (d)  $f_{\text{Sig5}}(t)$  that consists of the three modes in (a), (b) and (c) which are expressed in Eq. (37).



**Fig. 13.** Comparisons between the analytical components of  $f_{\text{Sig5}}(t)$  (dashed lines) in Eq. (37) and decomposition results of  $f_{\text{Sig5}}(t)$  (solid line) by the (a) EFD, (b) EWT, (c) FDM-LTH, (d) FDM-HTL, (e) VMD, and (f) EMD.

mode with a frequency greatly larger than those of the closely-spaced modes is shown in Fig. 12(c). The signal  $f_{Sig5}(t)$  is sampled at a frequency of 50 Hz for 20 s and shown in Fig. 12(d).

The EFD, EWT, FDM-LTH, FDM-HTL, VMD, and EMD are used to decompose the sampled  $f_{\rm Sig5}(t)$ . Their results are shown in Fig. 13 and corresponding RMSEs in Eq. (36) are calculated and listed in Table 4. Note that in the decomposition result by the FDM-LTH, only two components are obtained as  $f_{\rm Sig5C2}$  and  $f_{\rm Sig5C2}$  exist in the first component and RMSEs corresponding to  $f_{\rm Sig5C2}$  and  $f_{\rm Sig5C2}$  are mixed as one mode. For  $f_{\rm Sig5C1}$ , the RMSE associated with the FDM-HTL is the smallest and those associated with the VMD and EFD are relatively small, and those associated with the EWT, FDM-LTH and EMD are large. For  $f_{\rm Sig5C2}$ , similar observations can be obtained: the RMSE associated with the FDM-HTL is the smallest, those associated with the VMD and EFD are relatively small, and those associated with EWT, FDM-LTH and EMD are large. For  $f_{\rm Sig5C3}$ , the RMSEs associated with the FDM-HTL are the smallest and those associated with other methods are relatively small. It is indicated that the EFD yields decomposition results for signals with closely-spaced modes with higher accuracy than the EWT and EMD. In addition, the inconsistency between decomposition results by the FDM-LTH and FDM-HTL is verified again.

Another stationary signal with two modes [34] denoted by  $f_{\text{Sig6}}(t)$  is constructed to further compare performances of the different decomposition methods for signals with closely-spaced modes, which is expressed by

$$\begin{cases}
f_{\text{Sig6C1}}(t) &= \cos(2\pi t) \\
f_{\text{Sig6C2}}(t) &= a\cos(2\pi \lambda_r t) \\
f_{\text{Sig6}}(t) &= f_{\text{Sig6C1}}(t) + f_{\text{Sig6C2}}(t)
\end{cases}$$
(38)

where a and  $\lambda_r$  denote a ratio between the amplitudes of  $f_{\mathrm{Sig6C2}}(t)$  and  $f_{\mathrm{Sig6C1}}(t)$  and that between the frequencies of  $f_{\mathrm{Sig6C2}}(t)$  and  $f_{\mathrm{Sig6C2}}(t)$  and  $f_{\mathrm{Sig6C2}}(t)$  and  $f_{\mathrm{Sig6C2}}(t)$  and  $f_{\mathrm{Sig6C2}}(t)$  and  $f_{\mathrm{Sig6C2}}(t)$  become closely-spaced modes. The signal  $f_{\mathrm{Sig6}}(t)$  is sampled at a frequency of 10 Hz for 300 s. The EFD, EWT, FDM-LTH, FDM-HLT, VMD and EMD are deployed to decompose  $f_{\mathrm{Sig6}}(t)$ . A two-dimensional binary quantity  $Q(a,\lambda_r)$  is used to measure the decomposition performance [34] of the different methods for  $f_{\mathrm{Sig6}}(t)$  with different values of a and a, and it is expressed by

$$Q(a, \lambda_r) = \begin{cases} 0 & \text{if } \frac{\|\text{C}1 - f_{\text{Sig6C1}}\|_2}{\|f_{\text{Sig6C2}}\|_2} \leq \varepsilon \\ 1 & \text{if } \frac{\|\text{C}1 - f_{\text{Sig6C1}}\|_2}{\|f_{\text{Sig6C2}}\|_2} > \varepsilon \end{cases}$$
(39)

where C1 is the decomposed component by a decomposition method corresponding to  $f_{\text{Sig6C1}}(t)$  and  $\varepsilon$  is the threshold of Q. A zero value and a unit value of Q indicate an acceptable decomposition result and an unacceptable decomposition one, respectively, and the value of  $\varepsilon$  is chosen to be 0.5 in this study, which was also the case in Refs. [4,15,34]. Resulting  $Q(a, \lambda_r)$  corresponding to the six methods are shown in Fig. 14, where the colors of blue and yellow correspond to Q values of 0 and 1, respectively. It can be seen that the yellow area corresponding to the EFD is the smallest among the six Q results. Even as  $\lambda_r$  approaches to 1,  $f_{\text{Sig6}}(t)$  can still be well decomposed. However, the decomposition by the EFD is affected when a approaches to 0.01. Further, the yellow area corresponding to the EWT is the second smallest but its decomposition performance is affected when a approaches to 0.01 and  $\lambda_r$  is larger than 0.8. The yellow area corresponding to the VMD is the third smallest. Similar to Q corresponding to the EFD, as  $\lambda_r$  approaches to 1,  $f_{\text{Sig6}}(t)$  can still be well decomposed. However, the decomposition performance associated with the VMD is affected when a is close to 0.01 and 100. The yellow area corresponding to the EMD is the fourth smallest. The EMD cannot decompose  $f_{\text{Sig6}}(t)$ , when  $\lambda_r$  is larger than 0.65 for all a. In addition, worse decomposition results are obtained when a approaches to 100. For the FDM-LTH and FDM-HTL, decomposition performances are almost the same but the worst among the six methods. Their decomposition results are greatly affected by the value of a. They hardly decompose  $f_{\text{Sig6}}(t)$ , when a is smaller than 1 for  $\lambda_r \geqslant 0.01$ . Based on the observations, it is indicated that the EFD robustly and accurately decomposes  $f_{\text{Sig6}}(t)$  as its decomposition results are the most accurate even when  $f_{\text{Sig6}}(t)$  becomes a signal with closely-spaced modes, and both the FDM-LTH and FDM-HTL yield inaccurate decompo

# 4.4. TFR

TFRs of  $f_{Sig3}(t)$  of components decomposed by the six methods are compared to further study their performances. TFR of decomposed components by the EFD, EWT, VMD and EMD are calculated using Hilbert transform and those by the FDM-HTL, FDM-

**Table 4** Results of the RMSEs for  $f_{Sig5}(t)$ .

Component		Decomposition method					
	EFD	EWT	FDM-LTH	FDM-HTL	VMD	EMD	
$f_{ m Sig4C1}$	$2.20\times10^{-2}$	$1.11\times10^{-1}$	$7.07\times10^{-1}$	0.00	$1.90\times10^{-2}$	$7.02\times10^{-1}$	
$f_{ m Sig4C2}$	$1.60\times10^{-2}$	$1.10\times10^{-1}$	$7.07\times10^{-1}$	0.00	$1.50\times10^{-2}$	$6.94\times10^{-1}$	
$f_{ m Sig4C3}$	$1.20\times10^{-2}$	$1.20\times10^{-2}$	0.00	0.00	$1.41\times10^{-2}$	$4.58\times10^{-2}$	

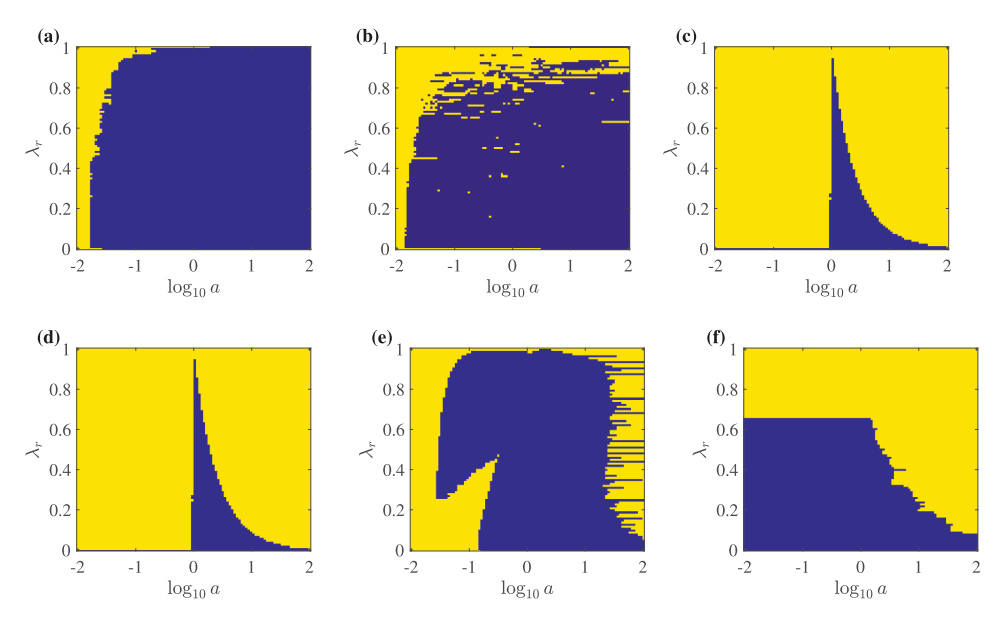


Fig. 14. Decomposition performance with respect to  $(a, \lambda_r)$  by the (a) EFD, (b) EWT, (c) FDM-LTH, (d) FDM-HTL, (e) VMD and (f) EMD.

LTH and FDM-DCT [35] are directly obtained as instantaneous amplitude and frequency. For the FDM-DCT, two frequency ranges of [0, 8] Hz and [8, 500] Hz are selected for  $f_{\text{Sig3}}(t)$  here, while a selection of frequency ranges for decomposition is not required by the other compared methods. A benchmark TFR is obtained by using Hilbert transforms of theoretical components. TFRs corresponding to seven decomposition methods and the benchmark one are shown in Fig. 15 and RMSEs corresponding to TFR are calculated and listed in Table 5. From Fig. 15, it can be found that the TFRs associated with the EFD and FDM-DCT compare well with the benchmark one, while the comparisons between the TFRs associated with the EWT, FDM-LTH and EMD and the benchmark one are acceptable. However, large differences can be observed for the TFRs corresponding to the VMD and FDM-HTL with the benchmark one.

In addition, RMSEs of between magnitudes in the TFRs by the seven methods and those in the benchmark TFR at all frequencies and times are calculated and listed in Table 5. It can be seen that the RMSEs associated with the TFRs by the EFD and EWT are the smallest. Those associated with the TFR by the FDM-DCT and EMD are relatively small, while those associated with the TFRs by the FDM-LTH, FDM-HTL and VMD are large. The TFRs shown in Fig. 15 and the RMSEs in Table 5 show that the EFD yields accurate TFR, and the inconsistency between TFR results by the FDM-LTH and FDM-HTL is observed. Besides, it is observed that the FDM-DCT improves the accuracy of TFR compared with those by the FDM-LTH and FDM-HTL.

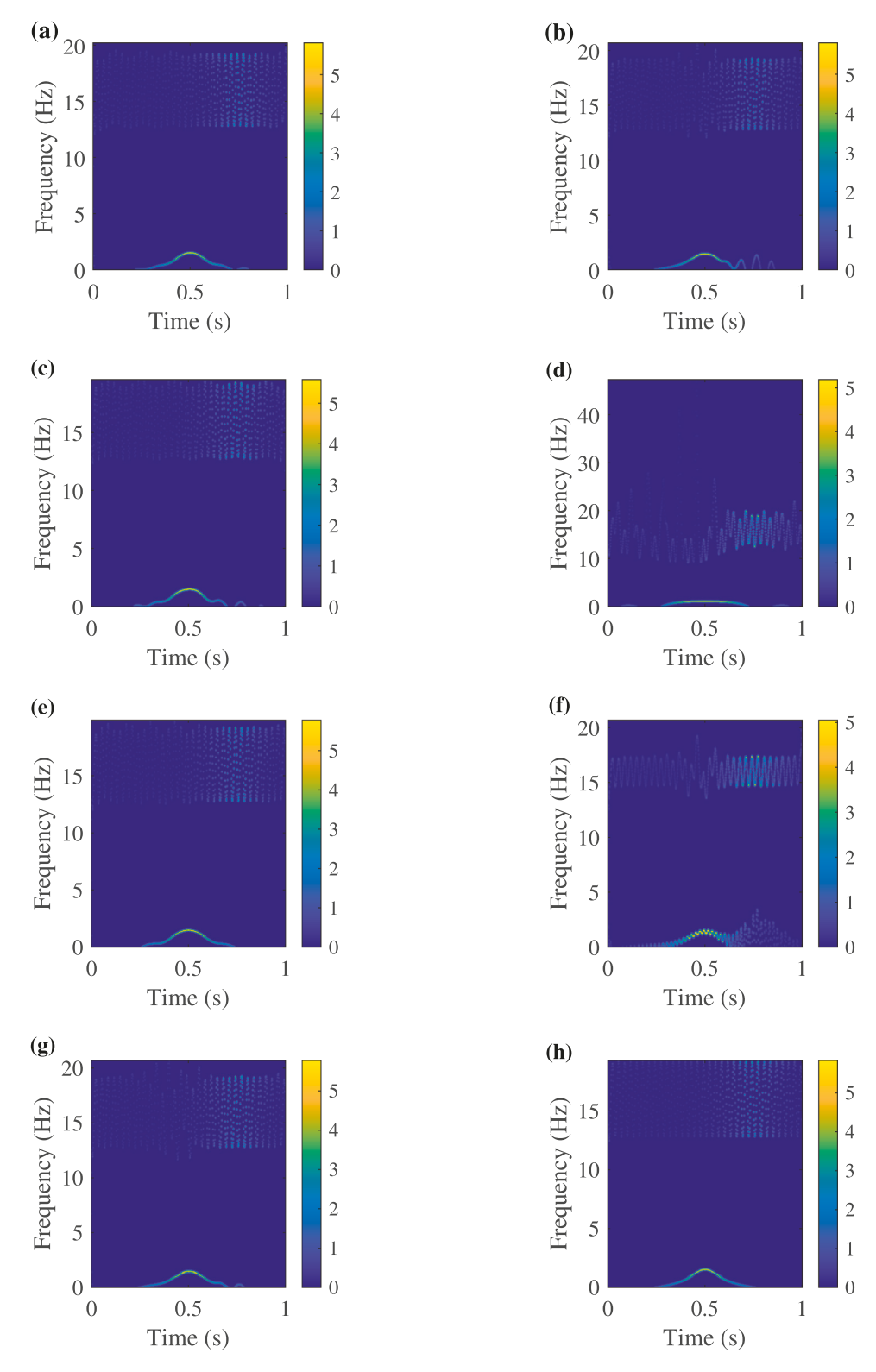
### 4.5. Computational cost

To explore the computational cost of the EFD, computation times by the EFD, EWT, FDM, VMD and EMD for  $f_{\text{Sig3}}(t)$ ,  $f_{\text{Sig4}}(t)$  and  $f_{\text{Sig5}}(t)$  are listed in Table 6. All computations are conducted on MATLAB R2020a on a PC with an Intel Xeon W-2123 CPU, 16.0 GB of RAM and 64-bit Windows 10. It can be seen that the EFD requires the shortest computation time among the six methods. The computation times associated with the EFD and EWT are comparable and while those of the FDM-HTL and FDM-LTW are large. The computational times of the VMD and EMD depended on their parameters; though they greatly vary, they are longer than that of the EFD. Hence, it can be concluded that the EFD is the most computationally efficient.

# 5. Experimental validation

In this section, an experimentally measured signal is used to validate the effectiveness of the proposed EFD. The signal was acquired from an experiment of the structural health monitoring benchmark problem in Refs. [36,37], where a four-story steel structure was tested. The structure had a height of 3.6 m and a square platform profile with an equilateral side length of 2.5 m, as shown in Fig. 16. More detailed descriptions of the benchmark problem and structure can be found in Ref. [36]. In one test case of the benchmark problem, two impacts were applied at the southeast corner of the first story of the structure in the north and west, i.e., along the *y*- and *x*-axes indicated in Fig. 16, respectively. Fifteen accelerometers were numbered and attached to measure the impact response of the structure with a sampling frequency of 1000 Hz. The accelerometer 15 measured the response of a point on the structure in the south, i. e., along the *y*-axis indicated in Fig. 16. Its measured response with a duration of 20 s was extracted after the first impact was applied. A low-pass filter with a cut-off frequency of 16 Hz was applied to the extracted response so that modal information associated with the first three modes of the structure could be reserved [38], and the filtered response is used for the validation here and shown in Fig. 17.

The filtered response is decomposed by the EFD, EWT, FDM-LTH, FDM-HTL, VMD, and EMD. Note that three, three and four components are predefined for the EFD, VMD and EWT, respectively. Decomposition results in the time- and frequency-domains by the



 $\textbf{Fig. 15.} \ \ \textbf{TFR results of} \ f_{Sig3}(t) \ \ \textbf{by: (a) EFD, (b) EWT, (c) FDM-LTH, (d) FDM-HTL, (e) FDM-DCT, (f) VMD, (g) EMD, and (h) benchmark.$ 

 Table 5

 Calculated RMSEs of TFR associated with  $f_{\text{Sig3}}(t)$ .

EFD	EWT	FDM-LTH	FDM-HTL	FDM-DCT	VMD	EMD
$1.00 \times 10^{-1}$	$1.01  imes 10^{-1}$	$1.27\times10^{-1}$	$1.36\times10^{-1}$	$1.12\times10^{-1}$	$1.33\times10^{-1}$	$1.13\times10^{-1}$

 $\textbf{Table 6} \\ \textbf{Computation time for } f_{\text{Sig3}}(t), \ f_{\text{Sig4}}(t) \ \text{and} \ f_{\text{Sig5}}(t) \ \text{by the EFD, EWT, FDM-LTH, FDM-HTL, VMD and EMD.}$ 

Signal	Computation Time (s)					
	EFD	EWT	FDM-LTH	FDM-HTL	VMD	EMD
$f_{\mathrm{Sig3}}(t)$	$1.66\times10^{-2}$	$6.33\times10^{-2}$	$1.75\times10^{-1}$	$1.09\times10^{-1}$	$1.75\times10^{-1}$	$8.21\times10^{-2}$
$f_{\mathrm{Sig4}}(t)$	$1.54\times10^{-2}$	$6.61\times10^{-2}$	$2.59\times10^{-1}$	$1.04\times10^{-1}$	$1.96\times10^{-0}$	$9.58\times10^{-2}$
$f_{\mathrm{Sig5}}(t)$	$1.67\times10^{-2}$	$7.02\times10^{-2}$	$1.59\times10^{-1}$	$1.16\times10^{-1}$	$1.41\times10^{-0}$	$1.51\times10^{0}$

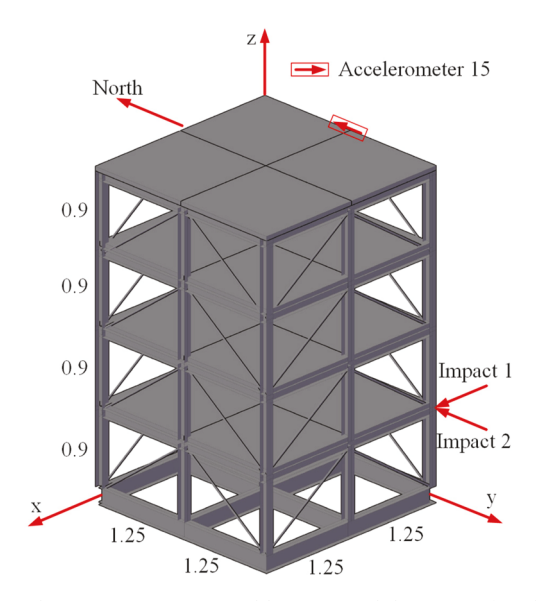


Fig. 16. Dimensions of the 4-story benchmark structure (unit: m), and locations and directions of applied impacts and response by the accelerometer 15.

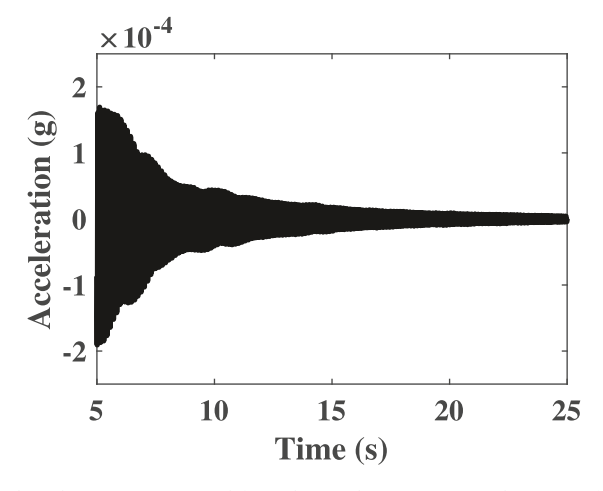


Fig. 17. Filtered response measured from the accelerometer 15 in the range of 5 to 25 s.

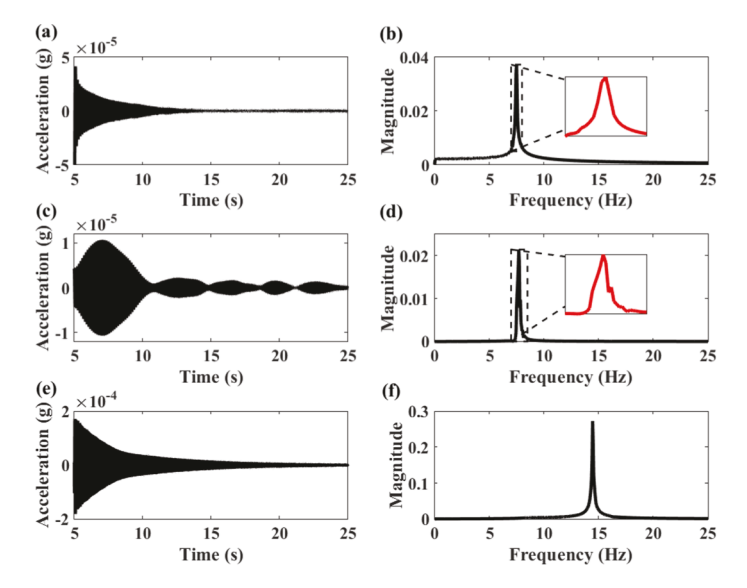


Fig. 18. Decomposition results by the EFD: (a) component 1 in time-domain, (b) component 1 in frequency-domain, (c) component 2 in time-domain, (d) component 2 in frequency-domain, (e) component 3 in time-domain and (f) component 3 in frequency-domain.

EFD, which correspond to the first three modes of the structure, are shown in Fig. 18. It can be observed that amplitudes of decomposed components 1 and 3 in the time-domain decay exponentially, while the amplitude of decomposed component 2 does not decay exponentially in a uniform manner might be due to the existence of measurement noise. Further, decomposition results in the frequency-domain show that the first two modes, which are considered closely-spaced, can be well decomposed by the EFD.

Decomposition results in the time and frequency-domains by the EWT are shown in Fig. 19. Similar to the decomposition results by the EFD, amplitudes of the decomposed components 1 and 3 in the time-domain by the EWT decay exponentially. But amplitudes of the decomposed component 2 in the time-domain does not decay exponentially in a uniform manner. Note that decomposed components 1 and 2 in the frequency-domain are different to those by the EFD, as shown in Fig. 20, where the mode-mixing problem occurs. In Fig. 20 (a), a frequency component, which corresponds to the component 2, exists in the frequency-domain decomposition result associated with the component 1. The issue is more obviously observed in Fig. 20(b): a frequency component, which corresponds to the component 1, exists with a high magnitude in the frequency-domain decomposition result associated with the component 2. Decomposition results in the time-domain and frequency-domain by the FDM-LTH, FDM-HTL, VMD and EMD are shown in Figs. 21–24, respectively. It can be observed that the two closely-spaced modes cannot be decomposed for the four methods. Besides, the decomposition result by the FDM-LTH, which corresponds to the component 1, is problematic due to the inclusion of the

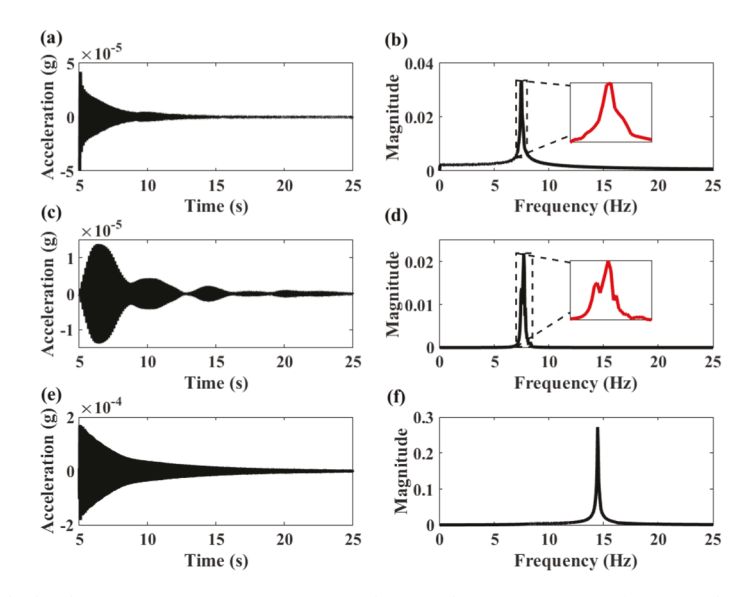


Fig. 19. Decomposition results by the EWT: (a) component 1 in time-domain, (b) component 1 in frequency-domain, (c) component 2 in frequency-domain, (d) component 2 in frequency-domain, (e) component 3 in frequency-domain.

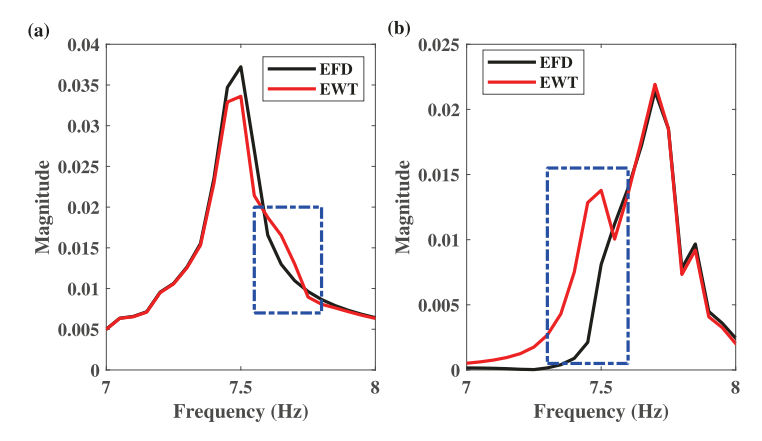


Fig. 20. Comparison of the components 1 and 2 of decomposition results by the EFD and EWT: (a) component 1 in frequency-domain and (b) component 2 in frequency-domain. The main difference between the decomposition results are boxed in blue.

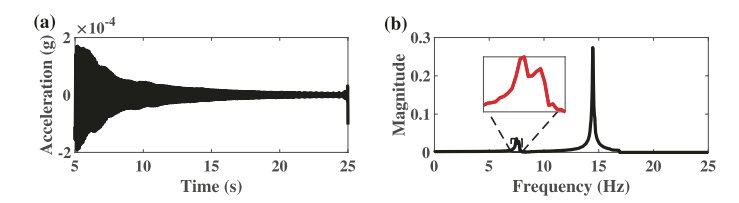


Fig. 21. Decomposition results by the FDM-LTH: (a) component 1 in time-domain and (b) component 1 in frequency-domain.

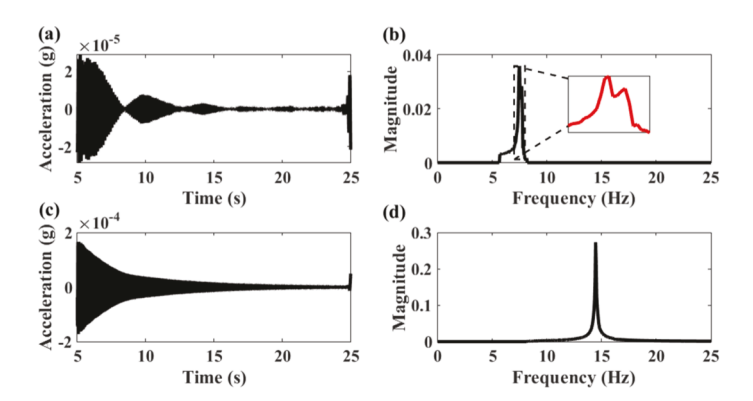


Fig. 22. Decomposition results by the FDM-HTL: (a) component 1 in time-domain, (b) component 1 in frequency-domain, (c) component 2 in time-domain and (d) component 2 in frequency-domain.

component 3. Results by the different decomposition method for the experimentally obtained data validate that the proposed EFD can yield the most accurate and robust decomposition results.

#### 6. Conclusion

In this paper, an accurate and efficient EFD method is proposed to decompose time-domain signals. The EFD consists of two critical steps: an improved segmentation technique and the construction of a zero-phase filter bank. In the improved segmentation technique, an adaptive sorting process is developed to yield accurate segmentation results and eliminate a possible trivial residual in the first decomposed component, which corresponds to the trivial component problem in the EWT. The use of the zero-phase filter bank facilitates accurate decomposition for signals with closely-spaced modes by eliminating transition phases that can cause the mode mixing problem in EWT. The inconsistency problem in FDM is solved by the segmentation technique, where the number of components in a signal to be decomposed is predefined. Two numerical investigations are conducted on non-stationary signals. It is shown that the EFD yields decomposition results with high accuracy and consistency. Two numerical investigations are conducted on two stationary signals to study the decomposition performance of the EFD for closely-spaced modes. It is shown that the EFD yields decomposition

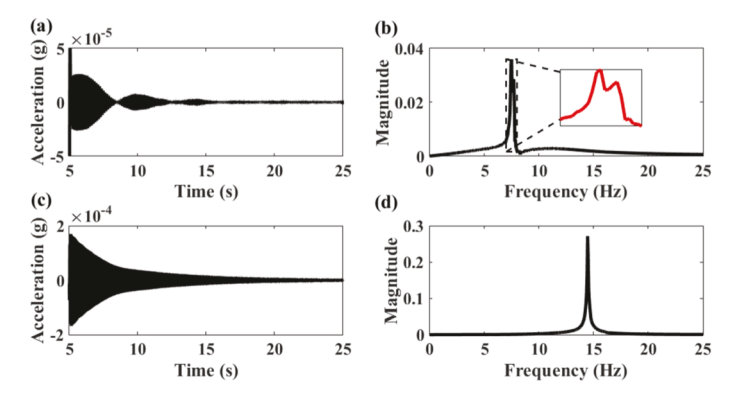


Fig. 23. Decomposition results by the VMD: (a) component 1 in time-domain, (b) component 1 in frequency-domain, (c) component 2 in time-domain and (d) component 2 in frequency-domain.

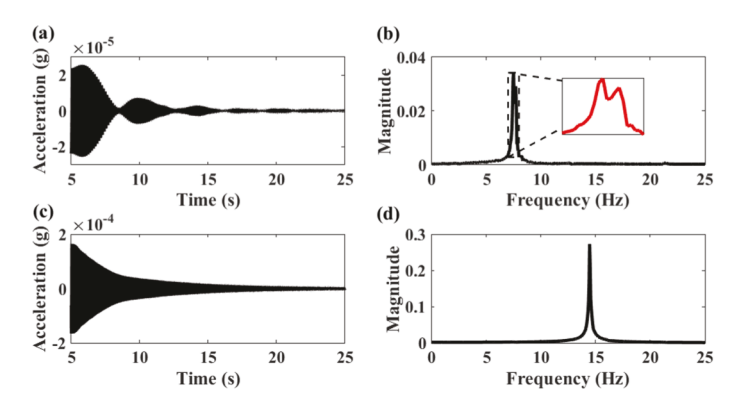


Fig. 24. Decomposition results by the EMD: (a) component 1 in time-domain, (b) component 1 in frequency-domain, (c) component 2 in time-domain and (d) component 2 in frequency-domain.

results for the closely-spaced modes with high accuracy and consistency and its decomposition results are more accurate than those by the other decomposition methods. In addition, it is shown that the EFD yields accurate TFRs for non-stationary signals. Comparisons between computation times by the EFD, EWT, FDM, VMD and EMD show that the EFD is the most computationally efficient. An experimental validation is also conducted using an experimentally acquired response from a benchmark problem. It is shown that the EFD can yield the most accurate decomposition results, compared with those by the other decomposition methods. However, a shortcoming of the EFD should be noted that signals with components crossing in the frequency domain cannot be decomposed accurately. The reason is that the improved segmentation method cannot differentiate such components at time instants when they cross in the frequency domain. A future work can be an investigation of the applicability of the EFD to signals/data of higher dimensions, such as digital images and vibration measurements by continuous scanning laser Doppler vibrometry. An implementation of the EFD along with code is available on GitHub. <sup>1</sup>

# CRediT authorship contribution statement

Wei Zhou: Conceptualization, Methodology, Software, Formal analysis, Visualization, Writing - original draft. Zhongren Feng: Supervision. Y.F. Xu: Methodology, Writing - review & editing, Funding acquisition, Resources, Project administration, Supervision. Xiongjiang Wang: Investigation, Writing - review & editing. Hao Lv: Writing - review & editing.

# **Declaration of Competing Interest**

The authors declare that they have no known competing financial interests or personal relationships that could have appeared to influence the work reported in this paper.

https://github.com/dopawei/EFD

## Acknowledgments

The authors Zhou and Xu are grateful for the financial support from the National Science Foundation through Grant No. CMMI-1762917. The authors gratefully acknowledge valuable discussions with and input from Dr. Gang Yu, Dr. Pushpendra Singh, Dr. Shiqian Chen and Dr. Heng Li. They also thank people who share their contributions to the signal processing community.

#### References

- A. Bhattacharyya, R.B. Pachori, A multivariate approach for patient-specific eeg seizure detection using empirical wavelet transform, IEEE Transactions on Biomedical Engineering 64 (9) (2017) 2003–2015.
- [2] F. Li, B. Zhang, S. Verma, K.J. Marfurt, Seismic signal denoising using thresholded variational mode decomposition, Exploration Geophysics 49 (4) (2018) 450-461
- [3] J. Pan, J. Chen, Y. Zi, Y. Li, Z. He, Mono-component feature extraction for mechanical fault diagnosis using modified empirical wavelet transform via data-driven adaptive Fourier spectrum segment, Mechanical Systems and Signal Processing 72 (2016) 160–183.
- [4] S. Chen, Y. Yang, Z. Peng, X. Dong, W. Zhang, G. Meng, Adaptive chirp mode pursuit: Algorithm and applications, Mechanical Systems and Signal Processing 116 (2019) 566–584.
- [5] A. Unadhyay, R. Pachori, Speech enhancement based on memd-ymd method, Electronics Letters 53 (7) (2017) 502–504.
- [6] D. Iatsenko, P.V. McClintock, A. Stefanovska, Nonlinear mode decomposition: a noise-robust, adaptive decomposition method, Physical Review E 92 (3) (2015), 032016
- [7] N.E. Huang, Z. Shen, S.R. Long, M.C. Wu, H.H. Shih, Q. Zheng, N.-C. Yen, C.C. Tung, H.H. Liu, The empirical mode decomposition and the hilbert spectrum for nonlinear and non-stationary time series analysis, Proceedings of the Royal Society of London. Series A: mathematical, physical and engineering sciences 454 (1971) (1998) 903–995.
- [8] G. Rilling, P. Flandrin, P. Goncalves, et al., On empirical mode decomposition and its algorithms, in: IEEE-EURASIP workshop on nonlinear signal and image processing, vol. 3, NSIP-03, Grado (I), 2003, pp. 8–11.
- [9] R. Rato, M.D. Ortigueira, A. Batista, On the hht, its problems, and some solutions, Mechanical Systems and Signal Processing 22 (6) (2008) 1374-1394.
- [10] Z. Wu, N.E. Huang, Ensemble empirical mode decomposition: a noise-assisted data analysis method, Advances in Adaptive Data Analysis 1 (01) (2009) 1–41.
- [11] M.E. Torres, M.A. Colominas, G. Schlotthauer, P. Flandrin, A complete ensemble empirical mode decomposition with adaptive noise, in: 2011 IEEE international conference on acoustics, speech and signal processing (ICASSP), IEEE, 2011, pp. 4144–4147.
- [12] J. Zheng, J. Cheng, Y. Yang, Partly ensemble empirical mode decomposition: An improved noise-assisted method for eliminating mode mixing, Signal Processing 96 (2014) 362–374.
- [13] X. Lang, N. ur Rehman, Y. Zhang, L. Xie, H. Su, Median ensemble empirical mode decomposition, Signal Processing 176 (2020) 107686.
- [14] D.P. Mandic, N. ur Rehman, Z. Wu, N.E. Huang, Empirical mode decomposition-based time-frequency analysis of multivariate signals: The power of adaptive data analysis, IEEE Signal Processing Magazine 30 (6) (2013) 74–86.
- [15] H. Li, Z. Li, W. Mo, A time varying filter approach for empirical mode decomposition, Signal Processing 138 (2017) 146-158.
- [16] K. Dragomiretskiy, D. Zosso, Variational mode decomposition, IEEE Transactions on Signal Processing 62 (3) (2013) 531-544.
- [17] M. Nazari, S.M. Sakhaei, Successive variational mode decomposition, Signal Processing 174 (2020), 107610.
- [18] S. McNeill, Decomposing a signal into short-time narrow-banded modes, Journal of Sound and Vibration 373 (2016) 325-339.
- [19] S. Chen, X. Dong, Z. Peng, W. Zhang, G. Meng, Nonlinear chirp mode decomposition: A variational method, IEEE Transactions on Signal Processing 65 (22) (2017) 6024–6037.
- [20] J. Gilles, Empirical wavelet transform, IEEE Transactions on Signal Processing 61 (16) (2013) 3999–4010.
- [21] Z. Luo, T. Liu, S. Yan, M. Qian, Revised empirical wavelet transform based on auto-regressive power spectrum and its application to the mode decomposition of deployable structure, Journal of Sound and Vibration 431 (2018) 70–87.
- [22] Y. Xin, H. Hao, J. Li, Operational modal identification of structures based on improved empirical wavelet transform, Structural Control and Health Monitoring 26 (3) (2019), e2323.
- [23] J.P. Amezquita-Sanchez, H. Adeli, A new music-empirical wavelet transform methodology for time–frequency analysis of noisy nonlinear and non-stationary signals, Digital Signal Processing 45 (2015) 55–68.
- [24] A. Bhattacharyya, L. Singh, R.B. Pachori, Fourier-bessel series expansion based empirical wavelet transform for analysis of non-stationary signals, Digital Signal Processing 78 (2018) 185–196.
- [25] P. Singh, S.D. Joshi, R.K. Patney, K. Saha, The Fourier decomposition method for nonlinear and non-stationary time series analysis, Proceedings of the Royal Society A: Mathematical, Physical and Engineering Sciences 473 (2199) (2017) 20160871.
- [26] P. Singh, Breaking the limits: redefining the instantaneous frequency, Circuits, Systems, and Signal Processing 37 (8) (2018) 3515-3536.
- [27] P. Singh, Novel Fourier quadrature transforms and analytic signal representations for nonlinear and non-stationary time-series analysis, Royal Society Open Science 5 (11) (2018), 181131.
- [28] I. Daubechies, Ten Lectures on Wavelets, SIAM, 1992.
- [29] J. Gilles, G. Tran, S. Osher, 2d empirical transforms. wavelets, ridgelets, and curvelets revisited, SIAM Journal on Imaging Sciences 7 (1) (2014) 157–186.
- [30] B. Picinbono, On instantaneous amplitude and phase of signals, IEEE Transactions on Signal Processing 45 (3) (1997) 552-560.
- [31] F.J. Harris, Multirate Signal Processing for Communication Systems, Prentice Hall PTR, 2004.
- [32] R.W.S. Alan, V. Oppenheim, Discrete Time Signal Processing, third ed., Prentice Hall, 2009.
- [33] T.Y. Hou, Z. Shi, Adaptive data analysis via sparse time-frequency representation, Advances in Adaptive Data Analysis 3 (01n02) (2011) 1–28.
- [34] G. Rilling, P. Flandrin, One or two frequencies? the empirical mode decomposition answers, IEEE Transactions on Signal Processing 56 (1) (2007) 85–95.
- [35] Pushpendra Singh, FDM based on DCT, DFT, FIR & FSAS, FEB 2020, type: dataset (2020). doi:10.13140/RG.2.2.30579.07203. http://rgdoi.net/10.13140/RG.2.2.30579.07203.
- [36] S.J. Dyke, D. Bernal, J. Beck, C. Ventura, Experimental phase ii of the structural health monitoring benchmark problem, in: Proceedings of the 16th ASCE Engineering Mechanics Conference, 2003.
- [37] D. Bernal, S.J. Dyke, H.F. Lam, J. Beck, Building Structural Health Monitoring Problem Phase 2 Experimental. URL: https://datacenterhub.org/dataviewer/view/neesdatabases:db/structura\_control\_and\_monitoring\_benchmark\_problems.
- [38] B. Alícíoğlu, H. Luş, Ambient vibration analysis with subspace methods and automated mode selection: case studies, Journal of Structural Engineering 134 (6) (2008) 1016–1029.